Title

Characterization of black carbon-containing particles from soot particle aerosol mass spectrometer measurements on the R/V
Atlantis
during CalNex 2010

Journal

Journal of Geophysical Research: Atmospheres, 120(6)

ISSN

2169897X

Authors

Massoli, Paola
Onasch, Timothy B
Cappa, Christopher D
et al.

Publication Date

2015-03-27

DOI

10.1002/2014JD022834

Peer reviewed

Characterization of black carbon-containing particles from soot particle aerosol mass spectrometer (SP-AMS) measurements on the *R/V* Atlantis during CalNex 2010

Paola Massoli[1], Timothy B. Onasch[1], Christopher D. Cappa[2], Ibraheem Nuamaan[3,4], Jani Hakala[5], Katherine Hayden[3], Shao-Meng Li[3], Donna T. Sueper[1,6], Timothy S. Bates[7,8], Patricia K. Quinn[8], John T. Jayne[1], and Douglas R. Worsnop[1]

[1] *Aerodyne Research Inc., Billerica, MA*

[2] *Department of Civil and Environmental Engineering, University of California, Davis, CA*

[3] *Air Quality Research Division, Environment Canada, Toronto, Canada*

[4] *Centre for Atmospheric Chemistry, York University, Toronto, Canada*

[5] *Department of Physics, University of Helsinki, Finland*

[6] *Department of Chemistry and Biochemistry, University of Colorado, Boulder, CO*

[7] *Joint Institute for the Study of the Atmosphere and Ocean, University of Washington, Seattle, WA*

[8] *NOAA Pacific Marine Environmental Laboratory, Seattle, WA*

Running Title: Properties of BC-containing particles

Corresponding author: Paola Massoli, Aerodyne Research Inc., Billerica., MA 01821, USA (pmassoli@aerodyne.com)

Abstract

We present mass spectrometry measurements of black-carbon containing particles made onboard the *R/V Atlantis* during the CalNex 2010 study using an Aerodyne Research Inc. soot particle aerosol mass spectrometer (SP-AMS). The *R/V Atlantis* was deployed to characterize air masses moving offshore the California coast and to assess emissions from sources in urban ports. This work presents a first detailed analysis of the size-resolved chemical composition of refractory black carbon (rBC) and of the associated coating species (NR-PM_{BC}). A co-located standard high resolution aerosol mass spectrometer (HR-AMS) measured the total non-refractory submicron aerosol (NR-PM_1). Our results indicate that, on average, 35% of the measured NR-PM_1 mass (87% of the primary and 28% of the secondary NR-PM_1, as obtained from the mass-weighted average of the NR-PM_{BC} species) was associated with rBC. The peak in the average size distribution of the rBC-containing particles measured by the SP-AMS in vacuum aerodynamic diameter (d_{va}) varied from ~100 nm to ~450 nm d_{va}, with most of the rBC mass below 200 d_{va}. The NR-PM_{BC} below 200 nm d_{va} was primarily organic, whereas inorganics were generally found on larger rBC-containing particles. Positive matrix factorization (PMF) analyses of both SP-AMS and HR-AMS data identified organic aerosol factors that were correlated in time, but had different fragmentation patterns due to the different instruments vaporization techniques. Finally, we provide an overview of the volatility properties of NR-PM_{BC} and report the presence of refractory oxygen species in some of the air masses encountered.

1. Introduction

Atmospheric aerosol particles have important impacts on visibility, human health, and climate [*Intergovernmental Panel on Climate Change* (*IPCC*)*,* 2013]. Refractory black carbon (rBC)-containing particles, often referred to as soot, are emitted from incomplete combustion processes, are strong light-absorbers in the visible and near visible wavelengths, and have been recognized as potentially important players in climate forcing through direct warming and alteration of cloud properties [*Jacobson,* 2001, 2006; *Ramanathan et al.,* 2007; *Ramanathan and Carmichael,* 2008; *Bauer et al.,* 2010; *Shindell et al.,* 2012; *Bond et al.,* 2007, 2013]. Understanding the transformations that rBC-containing particles undergo in the atmosphere after emission is key to accurately describing and modeling the radiative effects of rBC. It is well known that ageing of rBC can occur through coagulation and condensation of organic and inorganic components (or coating material), which can be mildly light absorbing or non-absorbing. As the coating thickness increases and evolves with ageing processes [e.g*., Riemer et al.,* 2010], the chemical and radiative properties of aged rBC particles can change dramatically compared to the ones of freshly emitted rBC [*Schnaiter et al.,* 2005; *Bond et al.,* 2006; *Stier et al.,* 2007; *Lack and Cappa,* 2010]. However, the complex nature of both fresh and aged rBC particles makes it challenging to describe their microphysics (e.g., mixing state), chemical (e.g., composition of coating) and optical (e.g., influence of coating on the magnitude of rBC absorption) properties. Recent studies have highlighted that the morphology of rBC-containing particles is likely very different than the "core-shell" structure that is typically assumed in many radiative models, and that rBC is not commonly located at the center but rather at the edge of an aerosol particle [*Adachi et al.,*

2010; *Sedlaceck et al.,* 2012, and references therein]. Such irregular morphologies may be the reason (or one of the reasons) for the smaller-than-predicted absorption enhancements recently observed for atmospheric rBC-containing particles in an urban environment [*Cappa et al.* 2012, and references therein]. Thus, there are still significant challenges related to understanding rBC properties and its effects on climate, as highlighted in a recent comprehensive review paper by *Bond et al.* [2013].

Extensive measurements of rBC mass loadings in different environments have taken place in the last two decades mainly by means of filter-based methods [*Metcalf et al.,* 2012, and references therein], which are relatively straightforward but do not provide information regarding the mass of the coating materials specifically associated with rBC particles. The introduction of the Single Particle Soot Photometer, SP2 [*Stephens et al.,* 2003], developed by Droplet Measurement Technologies (DMT), has represented a step forward in the characterization of rBC-containing particles, as the SP2 instrument allows for a real-time, sensitive quantification of rBC mass loadings and rBC-core size distributions on a single particle basis [*Stephens et al.* 2003; *Baumgardner et al.* 2004; *Schwarz et al.* 2006]. The SP2 also provides methods for estimating the thickness of the coating material associated with an rBC-core and the degree of mixing between core and coatings [e.g., *Gao et al.,* 2007; *Schwarz et al.,* 2008a, 2008b; *McMeeking et al.,* 2010; *Subramanian et al.,* 2010; *Metcalf et al.,* 2012]. However, the SP2 does not provide means to chemically speciate the coatings on rBC particles and is reliant on inversion methods to estimate the coating thickness. The Soot Particle Aerosol Mass Spectrometer (SP-AMS), recently developed by Aerodyne Research Inc. (ARI) [*Onasch et al.,* 2012], combines technologies from the DMT SP2 and the ARI high resolution aerosol mass

spectrometer (HR-AMS) [*DeCarlo et al.* 2006] to provide real-time and quantitative information on the mass loadings and size-resolved chemical composition of rBC-containing particles, i.e., rBC and associated non-refractory coating species.

Detailed measurements of the mass, size, chemical composition, and optical properties of rBC-containing particles were made as part of the California Research at the Nexus of Air Quality and Climate Change (CalNex) study onboard the *R/V* Atlantis in early summer 2010 (starting in San Diego on May 14, 2010, and ending in San Francisco on June 8, 2010). The CalNex 2010 effort aimed to better quantify pollutant emissions and understand key atmospheric chemistry issues related to both air quality and climate change in California [*Ryerson et al.,* 2013]. The megacity of Los Angeles (LA) has been historically characterized by air quality problems and severe pollution episodes due to a constantly growing number of pollutant sources combined with unique meteorological and geographic features that often favor pollution stagnation [*Lu and Turco*, 1995; *Angevine et al.,* 2012]. Despite significant improvements due to the state's efforts in reducing pollutant emissions, high levels of particulate matter (PM) are consistently recorded in the LA basin (www.arb.ca.gov/html/brochure/history). Many recent field campaigns have shown that the majority of PM in the LA Basin is nowadays represented by organic aerosols, OA [*Hayes et al., 2012*]; however, rBC emissions and concentrations in the LA area are still significant [*Metcalf et al.,* 2012].

As part of CalNex 2010, the *R/V* Atlantis was deployed to characterize air masses sampled along the California coast and to assess emissions from specific sources, e.g., ships in urban ports [*Buffaloe et al.,* 2014]. In addition to the *R/V* Atlantis, the study included two ground-based supersites (one at the California Institute of Technology

campus in Pasadena and one near Bakersfield, in the San Joaquin Valley), and multiple research aircraft [*Ryerson et al.,* 2013]. Onboard the *R/V* Atlantis, we deployed a suite of particle instruments to investigate the chemical composition, volatility, hygroscopicity and optical properties of the submicron aerosol, as well as changes in size, mass and chemical composition of rBC-containing particles as a function of atmospheric ageing. The implications of ageing on the optical properties of rBC-containing particles (i.e., effects on absorption enhancement due to rBC particle coatings) have been discussed in *Cappa et al.* [2012]. Here we focus on the chemical and physical measurements obtained using the SP-AMS instrument and describe the size and mass spectral differences of the various types of air masses encountered during the deployment. We present cases of coastal pollution events as the *R/V* Atlantis often sampled air masses as they moved offshore from the LA basin. In addition, the particulate volatilities of these aerosols are explored with the ARI thermal denuder (TD). We also discuss the results of positive matrix factorization (PMF) analyses of the SP-AMS data and compare these results with PMF performed on the data from a standard co-located HR-AMS.

2. Methods

2.1 Aerosol sampling and instrument setup

The aerosol sampling system on the *R/V* Atlantis during CalNex 2010 consisted of a 6 m long mast located 18 m above the ocean surface, and pointing forward of the ship's stack. Periods of self-sampling were eliminated based on the wind direction and wind speed data measured relative to the position of the inlet (a more complete description of the mast can be found in *Bates et al*. [2012]). During CalNex 2010, the sampling mast

144 was maintained at a relative humidity (RH) of 60% by controlling the mast temperature,
145 and particles were sent to a suite of instruments after passing through a PM_1 impactor and
146 an ARI thermal denuder, TD, that was similar in design and performance to that
147 described by *Huffman et al.* [2008]. Note that only the mast was kept at constant RH,
148 whereas the sampling lines delivering particles to the various instruments had no RH
149 control. The temperature in the heated section of the ARI TD was ramped between 30ºC
150 and 250ºC and back over a period of 90 minutes. The sample flow was alternated
151 between the unheated ("bypass mode") and heated ("TD mode") sections every 2.5
152 minutes [*Cappa et al.,* 2012]. The instruments located after the ARI TD included: a DMT
153 SP2 to measure single particle rBC mass and size; the ARI SP-AMS to measure the bulk
154 mass and chemical composition of both rBC and the coating associated with rBC
155 (hereafter NR-PM_{BC}) and their size distribution in the aerodynamic diameter (d_{va}) range
156 50-700 nm (*Canagaratna et al*., [2007], and references therein); a co-located standard
157 HR-AMS to measure the ensemble mass and chemical composition of the total non-
158 refractory PM_1 (NR-PM_1) and its size distribution in the same d_{va} range, 50-700 nm; a
159 Scanning Mobility Particle Sizer (SMPS, TSI Inc., Model 3936) to measure the aerosol
160 size distribution in the mobility diameter (d_m) range 20-600 nm, and the UC Davis Cavity
161 Ring-Down and Photo-Acoustic Spectrometers (CRD/PAS) to measure particle optical
162 properties (light absorption and extinction) as a function of RH [*Langridge et al.,* 2011;
163 *Lack et al.* 2012]. The University of Helsinki Volatility Hygroscopicity Tandem
164 Differential Mobility Analyzer (V-HTDMA) [*Villani et al.,* 2008], deployed to measure
165 the hygroscopic growth factors (GF) as a function of particle size, volatility, and RH,
166 sampled from the same PM_1 line but operated its own TD. A schematic of the

167 measurement setup on the *R/V* Atlantis is given in Figure 1. Additional details on each of
168 these instruments are provided in *Cappa et al.* [2012].
169
170 2.2 SP-AMS and HR-AMS measurements
171 The mass loadings and chemically resolved size distribution of rBC-containing
172 particles were directly measured via the ARI SP-AMS. The instrument operating
173 principles are discussed in *Onasch et al*. [2012]. The main feature of the SP-AMS is a
174 1064 nm continuous wave (CW) intra cavity laser (similar in design to the SP2 laser) that
175 is inserted into an HR-AMS chamber perpendicular to the particle beam axis. The laser
176 vaporizes absorbing rBC at the aerosol sublimation/incandescence temperatures (~ 4000
177 K). In the SP-AMS, particles are first aerodynamically focused into the laser beam. As
178 rBC-containing particles are heated by laser absorption, the coating material associated
179 with rBC is vaporized, generating neutral chemical species. The removal of the coating
180 allows the rBC core to heat up further and vaporize into neutral carbon clusters. The
181 resulting molecular vapor is ionized via 70 eV electron impact, and subsequent ion
182 detection and chemical characterization occur via standard high resolution mass
183 spectrometry [*Canagaratna et al.,* 2007]. The SP-AMS measures the chemical
184 composition and size distribution of both rBC and associated coating, NR-PM_{BC}, in the
185 sub-micron range (note that the size distribution is representative of the total particle, rBC
186 plus NR-PM_{BC}). We use the term NR-PM_{BC} to indicate the total coating material
187 measured by the SP-AMS - organics (ORG), sulfate (SO_4^{2-}), nitrate (NO_3^-), ammonium
188 (NH_4^+) and chloride (Chl^-) - which may include components that by definition are both
189 non-refractory and refractory, i.e., that vaporize in the laser below and above 600 ºC,

190 respectively. In fact, the higher temperature attained by laser heating extends the range of
191 detectable coating material associated with rBC [*Corbin et al.,* 2014].

192 The SP-AMS was calibrated for rBC quantification by determining the mass
193 specific ionization efficiency (mIE_{BC}), or instrument sensitivity, for size-selected Regal
194 Black particles [*Onasch et al.*, 2012]. The mIE_{BC} during CalNex 2010 was ~288
195 ions/picograms. The 3-σ detection limit for rBC was <0.1 μg m^{-3} for 60 s averaging. In
196 the SP-AMS, the collection efficiency (*CE*) for sampled particles, including the rBC and
197 NR-PM_{BC} components, depends on the extent of overlap between the particle beam and
198 the laser beam. If the ambient particle beam diverges more than the laser beam, the *CE*
199 will be less than unity. Therefore, in the case of the SP-AMS, the *CE* depends primarily
200 on the fraction of particles crossing the laser, and *CE* < 1 is likely due to losses of small
201 and non-spherical particles in the SP-AMS because of particle beam divergence [*Onasch*
202 *et al*., 2012]. Recent work by *Willis et al.* [2014] suggests that the *CE* due to particle
203 beam-laser beam overlap is similar for both rBC and NR-PM_{BC} components (i.e., the
204 same *CE* should be applied for all rBC-containing particle chemical components). Willis
205 et al. [2014] also note that the *CE* is dependent on the NR-PM_{BC} / rBC (coating-to-core)
206 ratio, or R_{BC}, where a larger *CE* is expected for more coated (larger and more spherical)
207 particles, which can focus more efficiently in the laser beam. Following *Willis et al.*
208 [2014], we derived an R_{BC}-dependent *CE* correction for the SP-AMS dataset (see Figure
209 S01 of supplementary material and related Text 02). During CalNex 2010, the *CE* was ~
210 0.6 on average, but varied from ~ 0.2 to 1.0 depending on the R_{BC} values. All the
211 SP-AMS data reported in this paper are corrected using this derived R_{BC} dependent *CE*.

212 The SPAMS was operated in the laser-only configuration (i.e., without tungsten
213 vaporizer) and in the *V* ion time of flight mode [*DeCarlo et al.,* 2006]. Note that in the
214 laser-only configuration, the SP-AMS selectively and exclusively detects particles that
215 absorb at 1064 nm, that is rBC, and its coating material NR-PM_{BC}. The data acquisition
216 alternated between mass spectrum (MS) and particle-time-of-flight (pToF) modes to
217 obtain mass loadings and chemically resolved average size distributions.

218 The co-located HR-AMS provided the chemical composition and size distribution
219 of NR-PM_1. The HR-AMS was operated in both *V* (high sensitivity, low mass resolution)
220 and *W* (lower sensitivity, higher mass resolution) modes [*DeCarlo et al.,* 2006], but only
221 the *V* mode data are used in this paper. The HR-AMS data were reported using a *CE* of
222 0.5 to account for particle bounce from the AMS vaporizer [*Matthew et al.,* 2008]. The
223 *CE* was obtained against comparisons with SO_4^{2-} concentrations on filter samples
224 analyzed by ion chromatography and checked against comparisons with a quadrupole
225 AMS [*Bates et al.*, 2012]. Because the aerosol was dried enough and particle sulfate was
226 neutralized, a particle phase-dependent *CE* correction [*Middlebrook et al.,* 2012] was not
227 necessary. Both SP-AMS and HR-AMS data were analyzed using the high resolution
228 AMS data analysis software package PIKA [*Sueper,* 2010]. Positive matrix factorization
229 (PMF) analyses were performed using the PMF2.exe algorithm (v.4.2) in robust mode
230 [*Paatero and Tapper*, 1994]. The PMF inputs (mass spectral and error matrices) were
231 prepared according to *Zhang et al.* [2011], and the solutions were evaluated with an Igor
232 Pro-based PMF Evaluation Tool (PET, v. 2.04), following the method described by
233 *Ulbrich et al.* [2009] and *Zhang et al.* [2011]. For both SP-AMS and HR-AMS data, the
234 elemental analysis (EA) was performed using the recently updated oxygen-to-carbon

(O/C) and hydrogen-to-carbon (H/C) ratios parameterization by *Canagaratna et al.* [2015a], which indicated that the standard analysis code of *Aiken et al.* [2007] can underestimate O/C and H/C by up to 30% and 10% respectively, especially for aerosol containing alcohol functional groups and dicarboxylic acids. All the data reported here are averaged to 10 minutes and do not include contributions from direct shipping emissions that are published elsewhere [*Cappa et al.,* 2014; *Buffaloe et al.,* 2014].

For the HR-AMS, the instrument uncertainty for the data reported in this paper is estimated to be +35/-15%. For the SP-AMS, the uncertainty in the mIE_{BC} calibration (i.e., rBC mass loading measurement) is approximately ±20%, based on the uncertainties in size selecting a single-sized mobility diameter with known mass, and counting the number concentration with a condensation particle counter (CPC). The uncertainty in the $mIE_{NR\text{-}PM_{BC}}$ calibration, estimated from mIE_{BC} and the relative ionization efficiency of rBC, RIE_{BC} (*Onasch et al.* [2012]), is approximately ±50%. The SP-AMS R_{BC}-dependent *CE* correction is based on a direct comparison with the co-located SP2 instrument, which has an estimated uncertainty of +100/-20%. Assuming that propagation of errors via addition in quadrature provides a useful error model, the combined mIE_{BC} and *CE* uncertainties suggest that the SP-AMS uncertainties are +100/-30% for rBC and +112/-54% for $NR\text{-}PM_{BC}$. These large uncertainties in the SP-AMS measurements are driven by the large SP2 uncertainties, which were unusually high for this study because of the instrument laser being misaligned (see full discussion in Text 01 of the supplement). For both SP2 and SP-AMS however, the precision is significantly higher than their corresponding absolute accuracies reported here.

3. Results and Discussion

3.1 Overview of the SP-AMS measurements

The *R/V* Atlantis cruise track is shown in Figure 2, color coded by the SP-AMS rBC mass loadings (left panel) and R_{BC} (right panel). The campaign average rBC mass loading was 0.3 μg m^{-3}, with generally higher values measured in Southern California than in Northern California. The highest rBC loadings were recorded downwind of the LA basin, in particular in the port area of Long Beach (~ 1 μg m^{-3}) and during periods when the *R/V* Atlantis sampled air masses coming from the LA urban area (rBC ~ 0.5 μg m^{-3}). Much lower rBC loadings (< 0.1 μg m^{-3}) were measured further away from the coast and/or when the air masses were influenced by clean marine air such as during the transit from Southern to Northern California. Typical rBC loadings measured in various Northern California locations (San Francisco Bay, Sacramento River) ranged from 0.1 to 0.25 μg m^{-3}. Similar to rBC, the largest R_{BC} values were recorded in Southern California (up to 25), but varied greatly with location with a campaign-average value around 10.

Figure 3 shows the high resolution time series of both rBC and its coating species (ORG, SO_4^{2-}, NO_3^-, NH_4^+, and Chl^-) measured by the SP-AMS. The campaign-average pie chart shows that the majority of the NR-PM_{BC} material associated with rBC was represented by ORG, followed by SO_4^{2-}. The mass loadings of NR-PM_{BC} were generally enhanced when sampling air masses coming from the urban LA area, which also coincide with periods of high optical extinction and absorption levels observed by the CRD/PAS system [*Cappa et al.,* 2012]. These time periods are highlighted in Figure 3, and listed in Table I. The three time periods highlighted by the solid boxes (labeled 1, 6 and 7) are chosen as case studies and will be discussed in section 3.2.

281 Figure 3 (bottom panels) also shows the SP-AMS chemically resolved average
282 particle time-of-flight (pToF) size distributions ($dM/d\log_{10}d_{va}$) of rBC and coating
283 species for Southern and Northern California. Similarly to *Massoli et al.* [2012], we use
284 the pToF of m/z 36 from unit mass resolution (UMR) data as a proxy for the rBC size
285 distribution because the C_3^+ at m/z 36 is the strongest carbon signal and has relatively
286 low interference from other particle components (Chl^- in this case). Still, the rBC size
287 distribution traces reported here are corrected for the Chl^- signal. The Chl^- contribution to
288 the m/z 36 pToF size distribution is estimated from $HChl_{37}$ - the isotope of $HChl_{35}$ at m/z
289 38, where all the pToF signal is attributable to $HChl_{37}$. After subtracting the estimated
290 Chl^- (i.e., the $HChl_{37}$ pToF trace multiplied by 3 to account for the isotopic ratio) from
291 the total m/z 36, we obtain a rBC pToF trace, and then we scale the integrated area to the
292 rBC mass concentration calculated from the high resolution analysis, so that the rBC size
293 distributions are quantitatively correct.
294 The pToF size distributions of Figure 3 show that, in general, most of the rBC
295 mass is centered around ~100-120 nm d_{va}; in the case of Southern California, however,
296 the pToF size distribution of rBC extends beyond 200 nm $d_{va,}$ and rBC is present up to
297 500-600 nm $d_{va,}$, indicating more compact rBC-containing particles at these larger sizes.
298 As for the coating species, ORG is present across the all size range in both cases
299 (although centered around 150 nm d_{va} in the Southern California case and ~100 nm d_{va} in
300 the Northern California case, thus very similar to the ~100 nm d_{va} rBC mode), while
301 SO_4^{2-}, NO_3^- and NH_4^+ are almost exclusively above 200 nm d_{va} and peak at ~400 nm d_{va}.
302 Chl^- was very low across the all d_{va} range throughout the CalNex campaign.
303

304 3.2 Measurements of urban air masses in Santa Monica Bay.

305 The *R/V* Atlantis spent a large fraction of the CalNex deployment (May 15-31,
306 2010) in the Santa Monica Bay to sample airmasses moving offshore from the LA urban
307 area under the land/sea breeze regime. Several pollution studies conducted in the LA area
308 in the last two decades have described in detail the meteorological phenomena that occur
309 in the southern California bight such as the Catalina eddy [*Angevine et al.,* 2013, and
310 references therein], often coupled with a local land/sea breeze circulation that is
311 characterized by a very weak night-time land breeze especially in the summer months [*Lu*
312 *and Turco*, 1995]. Polluted air transported from the LA urban core towards the ocean by
313 the night-time land breeze (hereafter "LA outflows") was sampled often by the *R/V*
314 Atlantis in various locations within the Santa Monica Bay, typically under conditions of
315 easterly-north easterly (E-NE), light winds (< 2 m s^{-1}) [*Wagner et al.,* 2012]. It is worth
316 noting that these air masses represent a multitude of emission sources that occur in the
317 LA urban area mainly during the day, and are pushed inland by the day time sea breeze
318 and then offshore by the nighttime land breeze (sometimes multiple times if rain or strong
319 winds are absent for a few consecutive days). As a result, these air mass were processed
320 by the time that they were measured by the *R/V Atlantis* located in the Santa Monica Bay.
321 The outflow events (c.f. Table I) generally lasted 5-8 hrs each, and were characterized by
322 enhanced rBC (up to 0.5-1 μg m^{-3}) and enhanced ORG in the SP-AMS NR-PM_{BC} and
323 ORG and SO_4^{2-} in the HR-AMS NR-PM_1. In some outflows, enhanced NO_3^- was also
324 observed in the SP-AMS NR-PM_{BC} (see Figure 3, middle panel). From the gas phase
325 standpoint, the LA urban outflows were characterized by increased CO, NO and NO_2,
326 and decreased O_3 [*Wagner et al.,* 2012, and references therein]. The mixing ratios of

many volatile organic compounds (VOCs) measured by proton transfer reaction time-of-flight mass spectrometry (PTR-ToF-MS) [*deGouw and Warneke,* 2007], i.e., acetaldehyde, acetone, formaldehyde, and aromatics (C_8 and C_9), were also slightly elevated in the outflows (see Figure S02 of supplementary material). Table 1 reports key parameters for the LA outflow events, including estimates of photochemical age (PCA) obtained as (-log([NOx]/[NOy]). As noted by *Cappa et al.* [2012], the dimensionless term (-log([NOx]/[NOy]) is a proxy for photochemical age and serves as a "clock" under the assumption that the conversion of NO_x into NO_y occurs at a rate equal to NO_2 + OH reaction rate. The PCA ranged from 0.05 to 0.45 for these outflow events, indicating fresh to moderately processed urban airmasses, while the oxygen-to-carbon ratio (O/C) obtained from the HR-AMS ranged from 0.43 to 0.69, and R_{BC} ranged from 2.5 to 25. In general, O/C and R_{BC} increased with PCA - as one expects with ageing - with the exception of the outflow cases of May 15 and May 16, which had the highest R_{BC} among these case studies, but lower PCA than other outflow events with lower R_{BC} (e.g., May 30 and 31). One possible explanation for this result is the sampling location: in fact, the sampling of May 15 and 16 occurred very close to the coastline in the Santa Monica Bay, whereas on May 30 and 31 the ship was further away from the coast, and at the edges of the Santa Monica Bay (offshore Palos Verdes and Ventura, respectively). Although it has been shown that the polluted urban air from LA carried by the land / sea breeze regime can reach well beyond the Santa Monica Bay [*Wagner et al.,* 2012, and references therein], differences in location and distance from the coastline - allowing mixing with more aged air masses - might have played a role, perhaps effecting PCA in a different manner than R_{BC}. The other - perhaps more likely - explanation is that May 15 (and May

16) represented "special cases". On May 15 - a Saturday - *Metcalf et al.* [2012] report aircraft measurements of a large increase of water soluble organic carbon (WSOC) relative to rBC (measured by an SP2) indicating SOA formation over the LA area, consistent with previous observations of SOA growth due to the so-called "weekend effect", a phenomenon resulting from the lack of fresh emission - mostly from diesel engines - during the weekends [*Metcalf et al.,* 2012; *Bahreini et al.,* 2012]. However, a similar build up of secondary material was not observed - at least at sea level - on the following weekend (May 21-22), when the LA outflow of May 21 exhibited lower PCA and R_{BC} than on May 15. Interestingly, the meteorological data indicate rain on May 18 and 19, which led to cleaner and perhaps less stagnant conditions in the following days.

In this section we look more in detail at the chemical composition and average pToF size distribution of three distinct air masses sampled in different locations within the Santa Monica Bay (highlighted in Figure 3 as events 1, 6 and 7). Figure 4 shows the SP-AMS chemically resolved pToF size distributions and the high resolution (HR) mass spectral profiles (MS) for the three case studies. The first case (panels a and b) shows airmasses sampled while the *R/V Atlantis* was in the Long Beach port area, thereby near direct emission sources. The second and the third cases are the outflows of May 29, 1500-2100 UTC (panels c and d) and of May 15, 1130-1700 UTC (panels e and f). In the pToF size distributions the total ORG is split between the two main OA types identified by PMF analysis, i.e., hydrocarbon-like (HOA) and oxygenated organic aerosol (OOA) factors, which are respectively used as proxies for fresh and more aged aerosol [*Zhang et al.*, 2005a]. The HOA and OOA pToF traces are obtained using the tracer-based method described by *Zhang et al.* [2005a, 2005c], i.e., using, respectively, the UMR pToF size

distributions at m/z 57 and m/z 44, and then scaling the integrated areas to the corresponding HOA and OOA mass loadings obtained by PMF analyses performed on the ORG matrix. The pie charts summarize the mass balance of the coating species.

The first case (#6 in Table I and Fig.3) is an example of fresh airmasses sampled in the Long Beach port. The pToF trace (Fig.4a) shows that the rBC size distribution is centered around 100 nm d_{va} ("fresh soot mode"), and the pie chart indicates that rBC represents almost 50% of the total mass measured by the SP-AMS. Similar to rBC, ORG is found below 200 nm $d_{va,}$ (although not completely internally mixed with rBC), and makes the majority of the measured NR-PM_{BC}; in this airmass, ORG is almost entirely made of HOA. Another small rBC mode peaking at 250 nm d_{va} (coated with HOA) is present. At larger d_{va}, there is additional rBC associated with small amounts of SO_4^{2-}, NO_3^-, and NH_4^+ (15% of the measured NR-PM_{BC}). In general, these pToF size distributions reveal a certain degree of external mixing between rBC and all of the NR-PM_{BC} species at both small and large $d_{va,}$, consistent with relatively fresh emissions. The HR MS of rBC and ORG for this case study is shown in Fig.4b, with rBC represented by the ion family C_x^+ and ORG represented by ions of the $C_xH_y^+$, $C_xH_yO_1^+$ and $C_xH_yO_{>1}^+$ families. From the MS of the C_x^+ ions we infer that most of the rBC signal (~90%) resides between C_1^+ (m/z=12) and C_5^+ (m/z=60), consistent with laboratory and previous ambient measurements [*Onasch et al.,* 2012; *Massoli et al.*, 2012; *Corbin et al.,* 2014] (see also Figure S03 of supplementary material for examples of rBC MS for different soot types). The C_3^+ cluster (m/z=36) is the most abundant rBC peak, followed by C_1^+ (m/z=12) and C_2^+ (m/z=24). The MS is dominated by the characteristic $C_xH_{2y-1}^+$

and $C_xH_{2y+1}^+$ ion pattern of "HOA-like" aerosol, with the signals at m/z=41, m/z=43 ($C_3H_7^+$, the highest peak of the MS), m/z=55 and m/z=57 being the dominant peaks.

The case study of May 29 (#7 in Table I and Fig. 3) is one of the outflow airmasses sampled in the LA basin. The pToF plot (Fig.4c) shows that most of the rBC mass is centered around the d_{va} ~100 nm "fresh soot mode", but a well defined rBC mode at ~ 400 nm d_{va} ("accumulation soot") is also present. ORG makes about 90% of the total measured coating mass, and it is largely made of HOA, similar to the previous case. However, compared to the first case study, here rBC amounts to 23% of the total measured mass, and it is more heavily coated even at larger d_{va}, suggesting some degree of air mass processing. The corresponding HR MS of rBC and ORG is shown in Fig.4d. As in the previous case, most of the rBC signal (~90%) resides between C_1^+ (m/z=12) and C_5^+ (m/z=60), and the MS is largely dominated by the $C_xH_y^+$ ion type. However, here about 70% of the signal at m/z=43 (the most intense peak in the MS) is $C_2H_3O^+$.

The third case (# 1 in Table I and Fig 3) represents a more processed air mass during the outflow of May 15. The pToF size distribution (Fig. 4c) shows that the majority of both rBC and NR-PM_{BC} mass are shifted to larger d_{va}, ~450 nm. rBC represents only 5% of the measured air mass, and it is coated by a much larger fraction of SO_4^{2-}, NO_3^-, NH_4^+ and Chl^- compared to the previous outflow case. In addition, almost 50% of ORG is represented by OOA. Despite the two outflow case studies having different size distributions and different R_{BC} and PCA (larger values for May 15, as discussed earlier), the difference in the MS is not as dramatic; however, oxygenated ions of the $C_xH_yO_1^+$ and $C_xH_yO_{>1}^+$ families are more abundant and make up a larger fraction of peaks such as m/z=41, m/z=43 (almost all $C_2H_3O^+$), m/z=55, m/z=71 and m/z = 85.

418 The HR-AMS pToF size distributions and HR MS of the ORG component for the
419 same three case studies are reported in Figure S04 of the supplementary material.
420 Generally, there is a good qualitative correspondence between SP-AMS and HR-AMS for
421 the pToFs in the average peak of the ORG and SO_4^{2-} size distributions, even though the
422 mass loadings are different and generally larger for the HR-AMS (particularly for the
423 inorganic species in the accumulation mode regions, e.g., SO_4^{2-}, NO_3^-, NH_4^+). One
424 interesting observation is that in all the three cases, the HR-AMS MS are dominated by
425 m/z=44 (CO_2^+), whereas the MS of the SP-AMS are dominated by m/z=43 ($C_3H_7^+$ and
426 $C_2H_3O_1^+$). Laboratory studies suggest that the SP-AMS provides vaporization of the NR-
427 PM_{BC} at lower temperatures compared to the standard tungsten vaporizer of the
428 HR-AMS, resulting in less overall fragmentation and therefore less CO_2^+ production in
429 the laser [*Onasch et al.,* 2012; *Canagaratna et al.,* 2015b]. The lower fragmentation also
430 explains the larger presence of ion fragments above m/z=100 in the SP-AMS spectra
431 compared to the HR-AMS spectra.
432
433 3.3 PMF analyses of SP-AMS and HR-AMS data
434 PMF analyses of the SP-AMS CalNex 2010 data were performed on the ORG
435 mass spectrum as well as on the combined mass spectral matrices of ORG and rBC
436 (ORG+rBC) in order to extract information on the fraction and typology of ORG
437 associated with rBC in different PMF factors. In this section we discuss the results of the
438 PMF performed on the ORG+rBC data, and compare them to the PMF analysis of the
439 HR-AMS ORG data. For the SP-AMS, we chose a 4-factor solution with rotational
440 forcing parameter fPeak = 0 ($Q/Qexp$ = 1.0), yielding a hydrocarbon-like OA component,

441 hereafter HOA+rBC, and three oxygenated OA components (OOA+rBC), two of which
442 were recombined. The choice of a 4-factor solution, as opposed to a 3-factor solution,
443 enabled the extraction of a more "standard" HOA MS (e.g., with m/z=44 lower than
444 m/z=43, and m/z=43 dominated by $C_3H_7^+$ rather than $C_2H_3O_1^+$). A detailed summary of
445 key diagnostic plots of the PMF results and a discussion of the factor solution choices for
446 the SP-AMS are reported in the supplementary material (Figures S05, S06, S07, S08 and
447 related text). For the HR-AMS, we also find that the data are best explained by a 4-factor
448 solution yielding an HOA and three OOA factors, two of which were recombined in a
449 similar way to the SP-AMS dataset.

450 Figure 5 presents the MS profiles and mass-weighted pie charts of the ion
451 components for the three PMF factors HOA+rBC, SV-OOA+rBC (obtained by
452 recombining two factors) and LV-OOA+rBC for the SP-AMS (left column) and HOA,
453 SV-OOA and LV-OOA for the HR-AMS (right column). The H/C and O/C values of the
454 PMF factors are also reported for both SP-AMS and HR-AMS. For the SP-AMS, the
455 HOA+rBC factor (panel 5a) is dominated by a characteristic $C_xH_{2y-1}^+$ and $C_xH_{2y+1}^+$ ion
456 pattern, with the ions $C_3H_7^+$ (m/z=43), $C_4H_7^+$ (m/z=55) and $C_4H_9^+$ (m/z=57) being the
457 dominant $C_xH_y^+$ peaks. The rBC (represented by the ion family C_x^+) accounts for ~60%
458 of the total HOA+rBC component mass concentration. The $C_xH_yO_1^+$ and the $C_xH_yO_{>1}^+$
459 ion families represent less than 20% of the total HOA+rBC mass. In the other two
460 factors, rBC is about 15% of the total mass. SV-OOA+rBC (panel 5b) is less oxygenated
461 than LV-OOA+rBC (panel 5c), which has the smallest fraction of $C_xH_y^+$ ions and the
462 largest fraction of $C_xH_yO_{>1}^+$ ions among the three factors. The O/C and H/C values
463 reported for the ORG component factors reflect this trend, with highest O/C and lowest

464 H/C for the LV-OOA+rBC. Both SV- and LV-OOA+rBC show a small, yet significant,
465 presence (~5% of the total mass) of $C_xH_yO_zS^+$ (organosulfates, mainly $CH_3SO_2^+$),
466 C_xH_yNz, (amines) and $C_xH_yN_zO_1^+$ (organonitrate) ions, which have been detected in
467 previous HR-AMS datasets [*Farmer et al.,* 2010]. During CalNex 2010, N-containing
468 ions were more abundant in the SV-OOA+rBC, while S-containing ions were only found
469 in the LV-OOA+rBC factor. The same result applies to the HR-AMS.

470 Figure 5 shows that both the SV-OOA+rBC and LV-OOA+rBC MS are
471 dominated by the $C_2H_3O_1^+$ ion at m/z=43, whereas the HR-AMS LV-OOA (panel 5f) is
472 dominated by CO_2^+ at m/z=44, consistent with LV-OOA factors data from worldwide
473 locations [*Jimenez et al.*, 2009; *Ng et al*., 2010]. We already noted in the discussion of
474 Figure 4 and S04 that this result is most likely related to differences in the fragmentation
475 pattern of the SP-AMS compared to the standard HR-AMS because of the different
476 vaporization scheme (laser vs. tungsten vaporizer), as supported by the recent work of
477 *Canagaratna et al.* [2015b]. To account for the differences in mass spectral
478 fragmentation pattern, the SP-AMS H/C and O/C (calculated excluding rBC) are adjusted
479 according to the SP-AMS-specific EA correction reported by *Canagaratna et al.* [2015b].
480 After this correction, the SP-AMS H/C values are 10-15% higher and the O/C values are
481 15-20% lower than the ones calculated for the HR-AMS factors.

482 Figure 6 shows the comparison between the SP-AMS and HR-AMS PMF factor
483 time series (TS). The high correlation between the time series (r^2 values are 0.8, 0.85 and
484 0.70 for the HOA, SV-OOA and LV-OOA factor pairs, respectively) indicate that the two
485 instruments find virtually identical factor solutions. The high correlation between the
486 HR-AMS PMF factors with ambient spectra from the high-resolution AMS database (see

487 http://cires.colorado.edu/jimenez-group/HRAMSsd and *Ulbrich et al.* [2009]) supports
488 this interpretation, with r^2 values of 0.98, 0.81 and 0.85 between our HR-AMS PMF
489 factors and the database for the HOA, SV-OOA and LV-OOA factors, respectively.

490 Figure 7 (top panel) shows the comparison between ambient SP-AMS NR-PM_{BC}
491 and ambient HR-AMS NR-PM_1, and the time series of the NR-PM_{BC} / NR-PM_1 (the
492 fraction of NR-PM_1 associated with rBC) for the entire CalNex 2010 campaign. The
493 Figure also indicates the three case studies (1,6,7) discussed previously. Based on the
494 scatter plot (top panel, left), the fraction of the NR-PM_1 mass measured by the HR-AMS
495 that is associated with rBC is 35% on average, but it is greatly variable throughout the
496 campaign (0.05 to 0.8) as shown by the time series of the NR-PM_{BC} to NR-PM_1 ratio (top
497 panel, right). The bottom panel of Figure 7 instead shows the comparison between
498 SP-AMS and HR-AMS PMF HOA (left) and total OOA (right), color coded by PCA. For
499 this particular comparison we use the results from the PMF analysis performed only on
500 the ORG matrix of the SP-AMS data to allow a more direct comparison with the
501 HR-AMS PMF solutions. It is worth noting that the PMF analysis performed on the
502 SP-AMS ORG matrix yields virtually the same MS profiles and TS as obtained for the
503 ORG+rBC matrix (see Figure S09 for the complete TS comparison of the SP-AMS and
504 HR-AMS PMF factors with both PMF analyses performed on the ORG matrix). The
505 HOA comparison of Figure 7a yields a regression slope - solid line - of 0.87 (r^2 = 0.84),
506 suggesting that the ambient HOA during CalNex 2010 was almost entirely associated
507 with rBC and therefore detected by the SP-AMS. The color coding indicates that the
508 majority of HOA have PCA < 0.4, as expected due to the association of this factor with
509 fresh air masses. For reference, we also show the best-fit line from a similar comparison

510 on SP-AMS and co-located HR-AMS data collected during the NYC 2009 study [*Massoli*
511 *et al.,* 2012] for which the HOA comparison gave a correlation slope of 0.81 (dashed
512 line). In the OOA case, the correlation for CalNex yields a slope of 0.41 (r^2 = 0.84),
513 indicating that 41% of the measured total OOA was associated with rBC; for comparison,
514 this fraction was 35% during the NYC 2009 study.

515 Figure 8 shows further comparisons between the SP-AMS NR-PM_{BC} and
516 HR-AMS NR-PM_1 for the inorganic species NO_3^-, NH_4^+, Chl^- and SO_4^{2-}. The slopes
517 (solid lines) are 0.6, 0.26, 0.51 and 0.21 respectively, and indicate the fraction of the
518 NR-PM_1 that is detected by the SP-AMS as NR-PM_{BC}. The dashed lines represent the
519 slopes obtained from the SP-AMS and HR-AMS comparison during the NYC 2009 study
520 [*Massoli et al.,* 2012]. It appears that, in both campaigns, SO_4^{2-} and NH_4^+ are the
521 inorganic species least associated with rBC. The size distributions presented earlier show
522 that these components are typically found in the accumulation mode soot, also consistent
523 with previous results from typical HR-AMS ambient data [e.g., *Zhang et al.,* 2005b;
524 *Canagaratna et al.,* 2007]. It has to be noted for these scatter plots that the data points
525 above 0.5, 0.15 and 2 μg m^{-3} for the NH_4^+, Chl^- and SO_4^{2-} SP-AMS loadings,
526 respectively, lie slightly above the campaign average fit lines (the same is true for the
527 OOA loadings above 3 μg m^{-3} in Figure 7b). These points correspond to the outflows of
528 May 15 and 16, which had a much larger R_{BC} than the rest of the dataset. While there
529 does appear to be a consistent, general trend in the measured NR-PM_1 mass fractions
530 associated with rBC particles, it is not clear that these fractions need to remain constant
531 under all conditions. Thus, the apparent variable slopes in the correlations may be due to
532 different atmospheric conditions. It is also possible that the R_{BC} -dependent CE that we

apply to the data, defined as an average correction curve to the dataset (see Fig. S01) may not capture - or correct for - the entire data variability. At the moment this approach provides the best *CE* correction. In the future, SP-AMS measurements that also incorporate a direct measure of the changes in particle beam width with coating thickness using beam width probe (BWP) measurements - as done by *Willis et al.* [2014] - may allow to directly measure the degree of particle to laser beam overlap (effectively the *CE*), and correct for differences in sensitivities with particle coating more accurately.

In order to further support our estimates of total NR-PM_1 associated with rBC, we tried to extract the same information by using other data independently acquired during the CalNex 2010 campaign, in particular, data from the V-HTDMA housed in the same container and data from an SMPS system housed in another container therefore sampling from a different inlet line, both operating downstream of their own TD. The V-HTDMA was set to measure three dry particle sizes, 50, 100 and 145 nm d_m. The hygroscopic growth factors, GF, were measured at 90% RH. The TD was set to ramp the temperature up and down from 50°C to 280°C in a 45 min interval, and the size distribution scan for each size occurred in 240s with thermal denuder, and in 180s without. The V-HTDMA measurements indicate that, on average, about 20% of the selected particles - by number - were hydrophobic (GF =1), suggesting the presence of refractory material, e.g., rBC. When plotting the fraction of particles with GF =1 as a function of PCA (Figure 9, panel a), we observe that the vast majority of these particles fall in the region with PCA < 0.4, with very little variability related to the initial dry particle size. This result is consistent with the hydrophobic nature of freshly emitted rBC-containing particles.

555 The TD connected to the SMPS was operated at 230 ºC. The airstream was split into two
556 flows (ambient and denuded), dried with nafion driers before the denuder, and then
557 measured with two SMPSs. The TD was periodically operated at ambient temperature to
558 measure and correct for any sampling biases from the two SMPSs. The SMPS
559 study-averaged integrated volume, number and surface area concentrations for the
560 ambient and TD periods were used to calculate the ratio of the TD/ambient surface area
561 (SA) concentrations. We obtained an average spherical-particle surface area ratio
562 SA_{TD}/SA_{AMB} distributed around 0.30, or 30% (Figure 9, panel b), a median SA ratio of
563 0.18 and only a few data points with SA_{TD}/SA_{AMB} larger than 0.4. We note that thermally
564 denuded SMPS SA ratio results may be biased high because of the spherical particle
565 shape assumption and by the fact that the thermally denuded SMPS results may include
566 other refractory material such as sea-salt (although the sea-salt fraction in PM_1 is usually
567 very small); we therefore estimate that 30% represents an upper limit for the condensable
568 secondary NR-PM_1 material that would be associated with rBC particles. Overall, these
569 independently calculated numbers compare well with the measured fraction of particles
570 containing rBC as obtained from the comparison of the SP-AMS and HR-AMS data, i.e.,
571 35% as a campaign average (c.f. Fig. 7 top panel).
572
573 3.4 Thermal denuder measurements
574 The combination of the TD with the SP-AMS measurements allowed to obtain
575 chemically resolved volatility profiles of the sampled ambient particles through
576 evaporation of the NR-PM_{BC} material induced by heating. As described in detail by
577 *Cappa et al.* [2012], the particles sampled through the TD enter a heating stage, then pass

578 through a charcoal diffusion denuder stage to prevent recondensation of volatile gases.
579 During CalNex 2010, the flow rate through the TD was 1.5 lpm, corresponding to a
580 residence time in the entire heated section of 8.5 seconds. The temperature in the heated
581 section of the TD was ramped from 30ºC to ~220ºC and back over a period of 90
582 minutes. The sample flow was alternated between the unheated ("bypass mode") and
583 heated ("TD mode") sections every 2.5 minutes using two computer-controlled actuated
584 stem valves. A small flow (0.3 lpm) always passed through the line that was not in use to
585 allow the system to respond rapidly after switching between modes. Based on the
586 principle that rBC does not evaporate in the TD, the rBC measurements made using the
587 SP2 behind the TD allowed estimation of the rBC mass loss through the TD [*Huffman et*
588 *al.*, 2008]. The average temperature dependent transmission function (Tr), defined as the
589 ratio between the rBC mass after passing through the TD vs. bypass line [*Cappa et al.,*
590 2012], was $Tr = 0.95–0.00083*T_{TD}$ (°C), which compares very well with that estimated by
591 *Huffman et al.* [2008] for a typical distribution of ambient submicron particles. However
592 for this dataset, rather than using the average T-dependent transmission function, the
593 correction for particle losses was performed by normalizing the measured ambient and
594 TD NR-PM_{BC} data by the corresponding rBC mass loadings - a point-by-point correction
595 - in order to reduce the scatter in the resulting corrected data.

596 Figure 10 shows the average TD "thermogram" (i.e., the plot of the mass fraction
597 remaining after heating as a function of TD temperature) for the SP-AMS coating species
598 ORG, SO_4^{2-}, NO_3^- and NH_4^+ for the entire campaign (the volatility profile of Chl^- is not
599 shown because of the low signal-to-noise). The NO_3^- profile shows the highest volatility
600 of all coating species, with the remaining mass fraction (MFR) below 0.2 already at ~

150ºC. SO_4^{2-} is the least volatile component, with MFR > 0.8 up to 140ºC, followed by a rapid MFR drop to 0.2 between 150º and 180ºC. The initial decrease of the MFR SO_4^{2-} values between 50º and 100ºC followed by an increase between 100º and 150ºC is a feature that has been observed in previous ambient data and it has been attributed to physical changes in particle sulfate phase or morphology [*Huffman et al.,* 2008]. The ORG coating has intermediate volatility between SO_4^{2-} and NO_3^-, with a MFR value of 0.5 at 100ºC; however, the ORG MFR stays around MFR = 0.2 above 150ºC, indicating that some of the ORG is much less volatile than e.g., SO_4^{2-} and NO_3^- at those temperatures. Finally, the NH_4^+ thermogram shows lower volatility that ORG and NO_3^- at T < 150ºC, with a rapid drop afterwards. Comparison with previous literature data [*Huffman et al.,* 2009; *Docherty et al.,* 2011] indicates that the SP-AMS NR-PM_{BC} material evaporates similarly to the total NR-PM_1. For temperatures above 200°C, at least 80% of NR-PM_{BC} material is removed from the ambient rBC-containing particles.

As discussed in Cappa et al. [2012], significant charring can be excluded based on the fact that most of the NR-PM_{BC} components are evaporated before high temperatures are reached; for T > 200°C, the MFR values are < 0.2 and only a small fraction of the initial ORG (<5%) is potentially charred upon heating. Figure S10 shows the normalized, high-resolution SP-AMS mass spectra of rBC for the average ambient (top-left panel) and for thermally denuded data with T > 200°C (top-right panel). The distribution of the rBC C_n^+ ions and their relative intensities are overall similar, even if the abundances of C_2^+, C_4^+ and C_8^+ relative to of C_3^+ differ (e.g., C_2^+/C_3^+ is higher in the ambient case). The campaign average, chemically resolved pToF size distributions corresponding to ambient and thermal denuder conditions (T > 200°C) are also shown (bottom panels). The

624 aforementioned small fractions of ORG and SO_4^{2-} that remain at elevated temperatures
625 are observed in the accumulation mode of the thermally denuded pToF traces, consistent
626 with *Cappa et al.* [2013].

627 Figure 11 shows the thermograms of the rBC coating species ORG, SO_4^{2-}, NO_3^-,
628 NH_4^+ and Chl^- (panels a and b), CO_2^+ (panels c and d) and other key ions ($C_3H_7^+$, $C_4H_9^+$
629 and $C_2H_3O^+$, panels e and f) for the case studies of May 29 and May 15, 2010, that
630 represent examples of moderately aged and aged urban air masses, respectively (c.f.
631 Figure 4). The data from May 27 are not reported here because there were no thermal
632 denuder data collected during those times. The thermograms of the coating species are
633 similar in both cases, with the only exception for SO_4^{2-} which has a more pronounced
634 increase at 140 ºC in the case of May 15. Likewise, the volatility of the $C_3H_7^+$, $C_4H_9^+$ and
635 $C_2H_3O^+$ ions (where $C_2H_3O^+$ is the most abundant fragment in both mass spectra of Fig. 4,
636 panels d and f, respectively) is similar between the two cases. There is instead a striking
637 difference in the trend of the CO_2^+ ion, which decreases with T for the May 15 case
638 (where the fraction of CO_2^+ in the MS in Fig. 4d, fCO_2^+, is 0.05), but it remains almost
639 flat in the case of May 29 (for which $fCO_2^+ = 0.126$, c.f. Fig. 4f). In the attempt to
640 estimate the fraction of CO_2^+ that is refractory, we calculated a refractory CO_2^+
641 component (R-CO_2) using the correlation between the measured fragment CO_2^+ and rBC,
642 allowing estimation of the fraction of particle CO_2^+ that is associated with rBC. The
643 non-refractory component (NR-CO_2) is then obtained by subtracting R-CO_2 from the
644 measured CO_2^+. In the case of May 29 (Fig. 11c), the calculated NR-CO_2 fraction is
645 virtually zero and the measured CO_2^+ follows the trend of the calculated R-CO_2, whereas
646 on May 15 (Fig. 11d) the measured CO_2^+ follows the trend of the calculated NR-CO_2. We

647 interpret this result as an indication of the different nature (and volatility) of the CO_2^+
648 fragment depending on the type of airmass and coating material that is associated with
649 rBC. In the case of May 29, an example of relatively fresh emissions with the majority of
650 ORG coating represented by HOA, the CO_2^+ fragment likely originates from refractory
651 oxygen species that form during the oxidation of organic material on the rBC surface.
652 The existence of a refractory CO_2^+ fragment has been observed in the laboratory for
653 certain types of soot (rBC) particles such as those generated using a propane diffusion
654 flame [*Onasch et al*. 2012; *Corbin et al.,* 2014]. In the case of May 15, a more aged air
655 mass with ~ 50% of ORG represented by OOA, the CO_2^+ fragment follows the expected
656 trend based on previous HR-AMS observations [*Huffman et al.,* 2009] and it is probably
657 originated from oxidized organic material condensed onto pre-existing rBC particles.
658 Finally, we estimate the fraction of ORG that is purely non-refractory by
659 subtracting the contribution of the estimated R-CO_2 fraction to the total measured ORG,
660 which at 200 ºC has MFR values of 0.2 and 0.1 for May 29 and May 15, respectively.
661 The resulting ORGcorr (obtained as ORG minus R-CO_2) is shown in Figs. 11a and 11b.
662 In the case of May 29, the MFR of ORGcorr drops below the MFR of ORG starting at T
663 > 120 ºC, and it is significantly lower (45%) than ORG MFR at 200 ºC. On May 15, the
664 MFR of ORGcorr is "only" 25% lower than ORG MFR at 200 ºC, consistent with the
665 presence of less refractory organic material in this more aged airmass.
666
667 4. Summary and conclusions
668 We present measurements of black-carbon containing particles made during the
669 CalNex 2010 study onboard the *R/V Atlantis* for the period May 15 - June 8, 2010. An

ARI soot particle aerosol mass spectrometer (SP-AMS) provided detailed measurements of the size-resolved chemical composition of refractory black carbon (rBC) and the associated coating species. The peak in the average size distribution of the rBC as measured by the SP-AMS in vacuum aerodynamic diameter, d_{va}, varied from ~100 nm d_{va} (fresh rBC emissions) to ~450 nm d_{va} (accumulation mode rBC, typical of more processed rBC-containing air masses). In general, rBC was associated with an organic aerosol (ORG) coating. A co-located standard high resolution aerosol mass spectrometer (HR-AMS) measured the non-refractory portion of the submicron aerosol, or NR-PM_1. The combination of the two instruments allows an estimate of the fraction of the NR-PM_1 that is associated with rBC (or NR-PM_{BC}, when referring to the SP-AMS). Our results indicate that, on average, 35% of the NR-PM_1 mass was associated with rBC, with some variability observed upon source and coating species. Detailed comparisons between the SP-AMS NR-PM_{BC} and HR-AMS NR-PM_1 revealed that the SP-AMS detected most of the primary NR-PM_1 (87% of the HOA) and 28% of the secondary NR-PM_1, as obtained from the mass-weighted average of all the remaining NR-PM_{BC} species. Consistently, positive matrix factorization (PMF) analyses of both NR-PM_1 and NR-PM_{BC} indicates that rBC is mostly associated with hydrocarbon-like organic aerosol (HOA). PMF results from SP-AMS and HR-AMS compare well, though differences in the fragmentation pattern to due the different vaporization techniques (laser vs. tungsten vaporizer) can be observed. The use of the thermal denuder (TD) allowed investigation of the volatility of the coating material exclusively associated with rBC. The volatility properties of less oxidized masses indicate the presence of refractory organic material (detected as CO_2^+) associated with rBC. Additional field measurements and laboratory experiments will be

693 needed to improve our current understanding of the sources and properties of non-volatile
694 (refractory) oxygenated material associated with soot particles.
695
696
697
698
699
700
701
702
703
704
705
706
707
708
709
710
711
712
713
714
715

716 Acknowledgements

717

718 The authors thank the crew of the *R/V Atlantis*, and Derek Coffman and Drew Hamilton
719 of NOAA PMEL for their assistance and help during the project. Thanks to Eric Williams
720 and Brian Lerner (NOAA CSD) for sharing the CO, CO_2, NO_x, NO_y and O_3 data, and to
721 Alexander Vlashenko (Environment Canada) for sharing the VOC data. We thank
722 Manjula Canagaratna and Leah Williams for their useful comments. This project was
723 funded by the NOAA Global Climate Change Program (# NA09AR4310125 and
724 NA09OAR4310124), the California Air Resources Board, the National Center for
725 Environmental Research (NCER) at USEPA (RD834558), the Canadian Federal
726 Government (PERD Project C12.007) and NSERC. The SP-AMS instrument was
727 developed with funding from the US Department of Energy SBIR Program (# DE-FG02-
728 07ER8489009). This manuscript has not been reviewed by any of the funding agencies.
729 The results shown in the paper will be provided to the readers. The SP-AMS data can be
730 accessed via the data server of the Pacific Marine Environmental Laboratory, PMEL
731 (http://saga.pmel.noaa.gov/Field/CalNex/index.html). Other data and, if necessary, the
732 code used in obtaining the results presented here will be provided upon inquiring to the
733 corresponding author (pmassoli@aerodyne.com).

734

735

736

737

738

739

740 5. References

741

742 Adachi, K., S. H. Chung, and P. R. Buseck (2010), Shapes of soot aerosol particles and
743 implications for their effects on climate, *J. Geophys. Res.,* 115, D15206,
744 doi:10.1029/2009JD012868.

745

746 Aiken, A. C., P. F. DeCarlo, and J. L. Jimenez (2007), Elemental Analysis of Organic
747 Species with Electron Ionization High-Resolution Mass Spectrometry, *Anal. Chem.,* 79,
748 8350–8358, doi:10.1021/ac071150w.

749

750 Angevine, W. M., L. Eddington, K. Durkee, C. Fairall, L. Bianco, and J. Brioude (2012),
751 Meteorological model evaluation for CalNex 2010, *Monthly Weather Review,* 140 (12),
752 3885-3906, doi: 10.1175/MWR-D-12-00042.1.

753

754 Angevine, W. M., et al. (2013), Pollutant transport among California regions, *J. Geophys.*
755 *Res. Atmos.*, 118, 6750–6763, doi:10.1002/jgrd.50490.

756

757 Bahreini, R.**,** A.M. Middlebrook, J.A. de Gouw, C. Warneke, M. Trainer, C.A. Brock, H.
758 Stark, S.S. Brown, W.P. Dube, J.B. Gilman, K. Hall, J.S. Holloway, W.C. Kuster, A.E.
759 Perring, A.S.H. Prevot, J.P. Schwarz, J.R. Spackman, S. Szidat, N.L. Wagner, R.J.
760 Weber, P. Zotter, and D.D. Parrish (2012), Gasoline emissions dominate over diesel in
761 formation of secondary organic aerosol mass, *Geophys. Res. Lett.,* 39, L06805,
762 doi:10.1029/2011GL050718.

763

764 Bates, T. S., et al. (2012), Measurements of ocean derived aerosol off the coast of
765 California, *J. Geophys. Res.,* 117, D00V15, doi:10.1029/2012JD017588.

766

767 Bauer, S. E., S. Menon, D. Koch, T. C. Bond, and K. Tsigaridis (2010), A global
768 modeling study on carbonaceous aerosol microphysical characteristics and radiative
769 effects, *Atmos. Chem. Phys.,* 10, 7439–7456, doi:10.5194/acp-10-7439-2010.

770

771 Baumgardner, D., G. L. Kok, and G. Raga (2004), Warming of the Arctic lower
772 stratosphere by light absorbing particles, *Geophys. Res. Lett.,* 31, L06117,
773 doi:10.1029/2003GL018883.
774
775 Bond, T. C., G. Habib, and R. W. Bergstrom (2006), Limitations in the enhancement of
776 visible light absorption due to mixing state, *J. Geophys. Res.,* 111, D20211,
777 doi:10.1029/2006JD007315.
778
779 Bond, T. C. (2007), Can warming particles enter global climate discussions?, *Environ.*
780 *Res. Lett.,* 2(4), 045030, doi:10.1088/1748-9326/2/4/ 045030.
781
782 Bond, T. C.*,* et al. (2013), Bounding the role of black carbon in the climate system: A
783 scientific assessment*, J. Geophys. Res.,* 118*,* 5380–5552*, doi:*10.1002/jgrd.50171.
784
785 Buffaloe, G. M., et al. (2014), Black carbon emissions from in-use ships: a California
786 regional assessment, *Atmos. Chem. Phys.,* 14, 1881-1896, doi:10.5194/acp-14-1881-
787 2014.
788
789 Canagaratna, M. R., J. T. Jayne, J. L. Jiménez, J. D. Allan, M. R. Alfarra, Q. Zhang, T. B.
790 Onasch, F. Drewnick, H. Coe, A. Middlebrook, A. Delia, L. R. Williams, A. M.
791 Trimborn, M. J. Northway, P. F. DeCarlo, C. E. Kolb, P. Davidovits, and D. R. Worsnop
792 (2007), Chemical and microphysical characterization of ambient aerosols with the
793 Aerodyne aerosol mass spectrometer, *Mass Spectrom. Rev.,* 26, 185–222.
794
795 Canagaratna, M. R., J. L. Jimenez, J. H. Kroll, Q. Chen, S. H. Kessler, P. Massoli, L.
796 Hildebrandt Ruiz, E. Fortner, L. R. Williams, K. R. Wilson, J. D. Surratt, N. M.
797 Donahue, J. T. Jayne, and D. R. Worsnop (2015a), Elemental ratio measurements of
798 organic compounds using aerosol mass spectrometry: characterization, improved
799 calibration, and implications, *Atmos. Chem. Phys.* 15, 253-272, doi:10.5194/acp-15-253-
800 2015
801

802 Canagaratna, M. R., P. Massoli, E. Browne, J. Franklin, K.R. Wilson, T.B. Onasch, E.
803 Fortner, E. C. Kolb, J.T. Jayne, J.H. Kroll, and D. R. Worsnop (2015b), Chemical
804 compositions of black carbon particle cores and coatings via soot particle aerosol mass
805 spectrometry with photoionization and electron ionization, *J. Phys. Chem. A,* DOI:
806 10.1021/jp510711u
807
808 Cappa, C.D. et al. (2012), Radiative Absorption Enhancements Due to the Mixing State
809 of Atmospheric Black Carbon, *Science,* 337, 1078, DOI: 10.1126/science.1223447
810
811 Cappa, C.D. et al. (2013), Response to Comment on "Radiative Absorption
812 Enhancements Due to the Mixing State of Atmospheric Black Carbon", *Science* 339, 393,
813 DOI: 10.1126/science.1230260.
814
815 Cappa, C. D., et al. (2014), A case study into the measurement of ship emissions from
816 plume intercepts of the NOAA ship *Miller Freeman*, *Atmos. Chem. Phys.,* 14, 1337-1352,
817 doi:10.5194/acp-14-1337-2014.
818
819 Corbin, J. C., B. Sierau, M. Gysel, M. Laborde, A. Keller, J. Kim, A. Petzold, T.B.
820 Onasch, U. Lohmann, and A.A. Mensah (2014), Mass spectrometry of refractory black
821 carbon particles from six sources: carbon-cluster and oxygenated ions, *Atmos. Chem.*
822 *Phys.,* 14(5), 2591–2603, doi:10.5194/acp-14-2591-2014.
823
824 DeCarlo, P. F., Kimmel, J. R., Trimborn, A., Northway, M. J., Jayne, J. T., Aiken, A. C.,
825 Gonin, M., Fuhrer, K., Horvath, T., Docherty, K. S., Worsnop, D. R., and J. L. Jimenez
826 (2006), Field-Deployable, High-Resolution, Time-of-Flight Aerosol Mass Spectrometer,
827 *Anal. Chem.,* 78, 8281-8289.
828
829 de Gouw, J. and Warneke, C.: Measurements of volatile organic compounds in the earths
830 atmosphere using proton-transfer reaction mass spectrometry, *Mass Spectrom. Rev.* 26,
831 223–257, 2007.
832

833 Docherty, K. S., et al. (2011), The 2005 Study of Organic Aerosols at Riverside (SOAR-
834 1): instrumental intercomparisons and fine particle composition, *Atmos. Chem. Phys.,* 11,
835 12387-12420, doi:10.5194/acp-11-12387-2011.
836
837 Farmer, D. K., Matsunaga, A., Docherty, K. S, Surratt, J. D., Seinfeld, J. H., Ziemann, P.
838 J., and J. L. Jimenez (2010), Response of an aerosol mass spectrometer to organonitrates
839 and organosulfates and implications for atmospheric chemistry, *Proc. Natl. Acad. Sci.*,
840 107,15, 6670–6675, doi: 10.1073/pnas.0912340107.
841
842 Gao, R. S., Schwarz, J. P., Kelly, K. K., Fahey, D. W., Watts, L. A., Thompson, T. L.,
843 Spackman, J. R., Slowik, J. G., Cross, E. S., Han, J. H., Davidovits, P., Onasch, T. B.,
844 and D. R. Worsnop (2007), A novel method for estimating light-scattering properties of
845 soot aerosols using a modified single-particle soot photometer, *Aerosol Sci. Technol.,* 41,
846 125-135
847
848 Hayes, P. L., et al. (2013), Organic aerosol composition and sources in Pasadena,
849 California during the 2010 CalNex campaign, *J. Geophys. Res. Atmos.,* 118*,* 9233–9257*,*
850 *doi:*10.1002/jgrd.50530*.*
851
852 IPCC: Climate Change 2013 (2013), The Physical Science Basis. Contribution of
853 Working Group I to the Fifth Assessment Report of the Intergovernmental Panel on
854 Climate Change [Stocker, T.F., D. Qin, G.-K. Plattner, M. Tignor, S.K. Allen, J.
855 Boschung, A. Nauels, Y. Xia, V. Bex and P.M. Midgley (eds.)]. Cambridge University
856 Press, Cambridge, United Kingdom and New York, NY, USA, 1535 pp.
857
858 Jacobson, M. Z. (2001), Strong Radiative Heating due to the Mixing State of Black
859 Carbon in Atmospheric Aerosols, *Nature*, 409, 695-697.
860
861 Jacobson, M. Z. (2006), Effects of externally-through-internally-mixed soot inclusions
862 within clouds and precipitation on global climate, *J. Phys. Chem. A,* 110(21), 6860–6873,
863 doi:10.1021/jp056391r.

Jimenez, J. L., M. R. Canagaratna, N. M. Donahue et al. (2009), Evolution of Organic Aerosols in the Atmosphere, *Science,* 326, 1525–1529, doi:10.1126/science.1180353.

Huffman, J. A., Ziemann, P. J., Jayne, J. T., Worsnop, D. R., and J. L. Jimenez (2008), Development and Characterization of a Fast-Stepping/Scanning Thermodenuder for Chemically- Resolved Aerosol Volatility Measurements, *Aerosol Sci. Technol.,* 42, 395–407, doi:10.1080/02786820802104981

Huffman, J. A., Docherty, K. S., Aiken, A. C., Cubison, M. J., Ulbrich, I. M., DeCarlo, P. F., Sueper, D., Jayne, J. T., Worsnop, D. R., Ziemann, P. J., and J.L. Jimenez (2009), Chemically-resolved aerosol volatility measurements from two megacity field studies, *Atmos. Chem. Phys.,* 9, 7161-7182, doi:10.5194/acp-9-7161-2009.

Lack, D. A., and C. D. Cappa (2010), Impact of brown and clear carbon on light absorption enhancement, single scatter albedo and absorption wavelength dependence of black carbon, *Atmos. Chem. Phys*., 10, 4207–4220, doi:10.5194/acp-10-4207-2010

Lack, D. A., M. S. Richardson, D. Law, J. M. Langridge, C. D. Cappa, R. J. McLaughlin, and D. M. Murphy (2012), Aircraft Instrument for Comprehensive Characterization of Aerosol Optical Properties, Part 2: Black and Brown Carbon Absorption and Absorption Enhancement Measured with Photo Acoustic Spectroscopy, *Aerosol Sci. Technol., 46*(5), 555-568, doi:10.1080/02786826.2011.645955.

Langridge, J. M., M. S. Richardson, D. Lack, D. Law, and D. M. Murphy (2011), Aircraft Instrument for Comprehensive Characterization of Aerosol Optical Properties, Part I: Wavelength-Dependent Optical Extinction and Its Relative Humidity Dependence Measured Using Cavity Ringdown Spectroscopy, *Aerosol Sci. Technol., 45*(11), 1305-1318, doi:10.1080/02786826.2011.592745.

Lu, R., and R. P. Turco (1996), Ozone distributions over the Los Angeles Basin: Three dimensional simulations with the SMOG model, *Atmos. Env.*, *30*, 4155-4176.

Massoli, P., E. C. Fortner, M. R. Canagaratna, L. R. Williams, Q. Zhang, Y. Sun, J. J. Schwab, A. Trimborn, T. B. Onasch, K. L. Demerjian, C. E. Kolb, D. R. Worsnop, and J. T. Jayne (2012), Pollution gradients and chemical characterization of particulate matter from vehicular traffic near major roadways: results from the 2009 Queens College Air Quality study in NYC, *Aerosol Sci. Technol.*, 46, 1201−1218.

Matthew, B. M., A. M. Middlebrook, and T.B. Onasch (2008), Collection efficiencies in an Aerodyne aerosol mass spectrometer as a function of particle phase for laboratory generated aerosols, *Aerosol Sci. Technol.*, 42:11, 884-898, doi: 10.1080/02786820802356797

McMeeking, G. R., et al. (2010), Black carbon measurements in the boundary layer over western and northern Europe, *Atmos. Chem. Phys.,* 10, 9393–9414, doi:10.5194/acp-10-9393-2010

Metcalf, A. R., J. S. Craven, J. J. Ensberg, J. Brioude, W. Angevine, A. Sorooshian, H. T. Duong, H. H. Jonsson, R. C. Flagan, and J. H. Seinfeld (2012), Black carbon aerosol over the Los Angeles Basin during CalNex, *J. Geophys. Res.,* 117, D00V13, doi:10.1029/2011JD017255.

Middlebrook, A. M., R. Bahreini, J. L. Jimenez, and M.R. Canagaratna (2012), Evaluation of Composition-Dependent Collection Efficiencies for the Aerodyne Aerosol Mass Spectrometer using Field Data, *Aerosol Sci. Technol.,* 46:3, 258-271, DOI: 10.1080/02786826.2011.620041

Ng, N. L., et al. (2010), Organic aerosol components observed in Northern Hemispheric datasets from Aerosol Mass Spectrometry, *Atmos. Chem. Phys.,* 10, 4625-4641, doi:10.5194/acp-10-4625-2010.

925 Onasch, T. B., A. Trimborn, E. C. Fortner, J.T. Jayne, G. L. Kok, L. R. Williams, D. R.
926 Worsnop, and P. Davidovits (2012), Soot particle aerosol mass spectrometer:
927 development, application and initial validation, *Aerosol Sci. Technol.,* 46, 804-817,
928 doi:10.1080/02786826.2012.663948.
929
930 Paatero, P., and U. Tapper (1994), Positive matrix factorization: A non-negative factor
931 model with optimal utilization of error estimates of data values, *Environmetrics*, 5, 111-
932 126
933
934 Ramanathan, V., M. V. Ramana, G. Roberts, D. Kim, C. Corrigan, C. Chung, and D.
935 Winker (2007), Warming trends in Asia amplified by brown cloud solar absorption,
936 *Nature,* 448(7153), 575–578, doi:10.1038/nature06019.
937
938 Ramanathan, V., and G. Carmichael (2008), Global and regional climate changes due to
939 black carbon, *Nat. Geosci.,* 1(4), 221–227, doi:10.1038/ ngeo156.
940
941 Riemer, N., M. West, R.A. Zaveri, and R.C. Easter (2010), Estimating soot aging time
942 scales with a particle-resolved aerosol model, *J. Aerosol Sci.*, 41, 143-158, DOI:
943 10.1016/j.jaerosci.2009.08.009.
944
945 Ryerson, T. B., et al. (2013), The 2010 California Research at the Nexus of Air Quality
946 and Climate Change (CalNex) field study, *J. Geophys. Res.,* 118, 5830–5866,
947 *doi:*10.1002/jgrd.50331.
948
949 Schnaiter, M., C. Linke, O. Möhler, K. Naumann, H. Saathoff, R. Wagner, U. Schurath,
950 and B. Wehner (2005), Absorption amplification of black carbon internally mixed with
951 secondary organic aerosol, *J. Geophys. Res.,* 110, D19204, doi:10.1029/2005JD006046.
952
953 Schwarz, J. P., et al. (2006), Single-particle measurements of midlatitude black carbon
954 and light-scattering aerosols from the boundary layer to the lower stratosphere, *J.*
955 *Geophys. Res.,* 111, D16207, doi:10.1029/ 2006JD007076.

956 Schwarz, J. P., et al. (2008a), Measurement of the mixing state, mass, and optical size of
957 individual black carbon particles in urban and biomass burning emissions, *Geophys. Res.*
958 *Lett.*, 35, L13810, doi:10.1029/ 2008GL033968.
959
960 Schwarz, J. P., et al. (2008b), Coatings and their enhancement of black carbon light
961 absorption in the tropical atmosphere, *J. Geophys. Res*., 113, D03203,
962 doi:10.1029/2007JD009042.
963
964 Sedlacek, A. J., III, E. R. Lewis, L. Kleinman, J. Xu, and Q. Zhang (2012),
965 Determination of and evidence for non-core shell structure of particles containing black
966 carbon using the Single-Particle Soot Photometer (SP2), *Geophys. Res. Lett.,* 39, L06802,
967 doi:10.1029/2012GL050905.

968 Shindell, D., et al (2012), Simultaneously mitigating near-term climate change and
969 improving human health and food security, *Science*, 335, 183-189,
970 doi:10.1126/science.1210026.

971 Stephens, M., N. Turner, and J. Sandberg (2003), Particle identification by laser-induced
972 incandescence in a solid-state laser cavity, *Appl. Opt.,* 42(19), 3726–3736,
973 doi:10.1364/AO.42.003726.
974
975 Stier, P., J. H. Seinfeld, S. Kinne, and O. Boucher (2007), Aerosol absorption and
976 radiative forcing, *Atmos. Chem. Phys.,* 7, 5237–5261, doi:10.5194/acp-7-5237-2007.
977 Subramanian, R., et al. (2010), Black carbon over Mexico: The effect of atmospheric
978 transport on mixing state, mass absorption cross-section, and BC/CO ratios, *Atmos.*
979 *Chem. Phys.,* 10, 219–237, doi:10.5194/acp- 10-219-2010.
980
981 Sueper, D. (2010), ToF-AMS Analysis Software, available at:
982 http://cires.colorado.edu/jimenez-group/ToFAMSResources/ ToFSoftware/index.html.
983

984 Ulbrich, I. M., M.R. Canagaratna, Q. Zhang, D.R. Worsnop, and J.L. Jimenez (2009),
985 Interpretation of Organic Components from Positive Matrix Factorization of Aerosol
986 Mass Spectrometric Data, *Atmos. Chem. Phys*., 9, 2891-2918.
987
988 Villani, P., D. Picard V. Michaud, P. Laj, and A. Wiedensohler (2008), Design and
989 validation of a volatility hygroscopic tandem differential mobility analyzer (VH-TDMA)
990 to characterize the relationships between the thermal and hygroscopic properties of
991 atmospheric aerosol particles, *Aerosol Sci. Technol.,* 42, 729-741.
992
993 Wagner, N. L., et al. (2012), The sea breeze/land breeze circulation in Los Angeles and
994 its influence on nitryl chloride production in this region, *J. Geophys. Res*., 117, D00V24,
995 doi:10.1029/2012JD017810.
996
997 Willis, M. D., A. K. Y. Lee, T. B. Onasch, E.C. Fortner, L.R. Williams, A.T.
998 Lambe, D.R. Worsnop, and J. P. D. Abbatt (2014), Collection efficiency of the Soot-
999 Particle Aerosol Mass Spectrometer (SP-AMS) for internally mixed particulate black
1000 carbon, *Atmos. Meas. Tech.,* 7, 4507-4516, doi:10.5194/ amt-7-4507-2014.
1001
1002 Zhang, Q., M.R. Alfarra, D.R. Worsnop, J.D. Allan, H. Coe, M.R. Canagaratna, and J.L.
1003 Jimenez (2005a), Deconvolution and Quantification of Hydrocarbon-like and
1004 Oxygenated Organic Aerosols Based on Aerosol Mass Spectrometry, *Environ. Sci.*
1005 *Technol*., 39: 4938-4952, doi:10.1021/es048568l
1006
1007 Zhang Q, M.R. Canagaratna, J. T. Jayne, D.R. Worsnop, and J. L. Jimenez (2005b),
1008 Time and size-resolved chemical composition of submicron particles in Pittsburgh—
1009 Implications for aerosol sources and processes, *J. Geophys. Res.,* 110:
1010 doi:10.1029/2004JD004649.
1011
1012 Zhang, Q., D.R. Worsnop, M.R. Canagaratna, and J.L. Jimenez (2005c), Hydrocarbon-
1013 like and Oxygenated Organic Aerosols in Pittsburgh: Insights into Sources and Processes
1014 of Organic Aerosols., *Atmos. Chem. Phys*.,, 5, 3289-3311

Zhang, Q., J.L. Jimenez, M.R. Canagaratna., I.M. Ulbrich, N.L. Ng, D.R. Worsnop, and Y. Sun (2011), Understanding atmospheric organic aerosols via factor analysis of aerosol mass spectrometry: a review, *Anal. Bioanal. Chem,* 401:3045-3067, doi:10.1007/s00216-011-5355y.

1046 6. Tables

1047

Date, Time (UTC)	Sampling Location (air mass type)	R_{BC} (SP-AMS)	O/C (HR-AMS)	PCA
1) May 15, 1130-1700	Santa Monica Bay (night-time chemistry)	23	0.52	0.3
2) May 16, 0930-1500	Santa Monica Bay (night time chemistry)	24	0.64	0.32
3) May 21, 0930-1900	Santa Monica Bay (night time chemistry)	9	0.60	0.18
4) May 24, 0800-1700	Santa Monica Bay (offshore LAX)	2.5	n/a	0.05
5) May 25, 1230-1530	Santa Monica Bay (offshore LAX)	2.8	0.44	0.045
6) May 27, 0430-1100	Long Beach Port (fresh emissions)	3	0.35	0.03
7) May 29, 1500-2100	Santa Monica Bay (day time chemistry)	6.1	0.43	0.05
8) May 30, 0800-1130	Offshore Palos Verdes (night time chemistry)	10	0.66	0.45
9) May 31, 1030-2000	Offshore Ventura (night time chemistry)	10.8	0.69	0.43

1048

1049

1050 Table I: List of air masses sampled by the *R/V* Atlantis off the coast of Southern
1051 California, mainly in the Santa Monica Bay, during the CalNex 2010 research cruise. The
1052 cases highlighted in gray (1, 6, 7) are discussed in detail in the paper. The R_{BC} ratio (from
1053 the SP-AMS), the O/C ratio (from the HR-AMS) and the proxy for photochemical age
1054 PCA (-log([NOx]/[NOy])), are reported for each event.

1055

1056

7. Figure Captions

Figure 1: Schematic of the instrument setup described in this paper during the CalNex 2010 deployment (May 15-June 8, 2010) on the *R/V* Atlantis.

Figure 2: Left panel: SP-AMS rBC loadings (in μg m^{-3}) plotted along the *R/V* Atlantis cruise track. The highest rBC loadings were recorded nearby the Long Beach port areas. Right panel: SP-AMS R_{BC} (defined as NR-PM_{BC} / rBC) plotted along the cruise track. All data are averaged to 10 minutes.

Figure 3: Top panel: location (latitude vs. time) of the *R/V Atlantis* during CalNex 2010. Middle panel: Temporal series of rBC and NR-PM_{BC} species (ORG, SO_4^{2-}, NO_3^-, NH_4^+ and Chl^-) mass loadings measured by the SP-AMS. The sections highlighted in the solid boxes (labeled 1, 6, and 7) indicate the case studies described in section 3.2. The other dashed boxes highlight other LA outflow events sampled in the Santa Monica Bay (see Table I). Bottom panel: SP-AMS chemically resolved average pToF size distributions ($dM/d\log_{10}d_{va}$) of rBC and NR-PM_{BC} species for Southern and Northern California.

Figure 4: SP-AMS chemically resolved pToF size distributions ($dM/d\log_{10}d_{va}$), mass-weighted pie charts and high resolution mass spectral profiles (MS) of the ORG component for the three case studies of May 27 (panels a, b), May 29 (panels c, d) and May 15 (panels e, f). The HOA and OOA contributions to the total ORG pToF traces are shown. The average PCA and SP-AMS-based R_{BC} are reported for all cases.

Figure 5: Results of the PMF analyses performed on the combined ORG+rBC matrices from the SP-AMS (left) and on the ORG matrix for the HR-AMS (right). Mass-weighted pie charts of rBC and ORG ion families are shown for the SP-AMS HOA+rBC, SV-OOA+rBC, and LV-OOA+rBC factors. The HOA+rBC factor is dominated by CxHy, while the OOA factors have larger fractions of oxygenated ions. The O/C and H/C obtained with the new parameterizations by *Canagaratna et al.* [2015a, 2015b] are reported for both SP-AMS and HR-AMS.

Figure 6: Time-series illustrating the comparison between the SP-AMS (black traces) and HR-AMS PMF factors (color-coded traces). The comparison shows a good qualitative agreement, indicating that PMF finds similar solutions in both datasets. The r^2 between the PMF factors are 0.8 for HOA+rBC vs. HOA, 0.85 for SV-OOA+rBC vs. SV-OOA and 0.7 for LV-OOA+rBC vs. LV-OOA.

Figure 7: Top panel: Correlation plot of SP-AMS NR-PM_{BC} vs. HR-AMS NR-PM_1 (left), and time series of the NR-PM_{BC} to NR-PM_1 ratio (right). The average mass fraction of the measured NR-PM_1 that is associated with rBC is 0.35. Bottom panel: SP-AMS vs. HR-AMS comparison for the HOA and OOA components, color coded by PCA. The fit to the CalNex data is shown by solid lines. The slopes of the correlation, f(x), and the r^2 are also reported. The dashed lines indicate the fits to similar SP-AMS vs. HR-AMS correlations from the NYC 2009 study [*Massoli et al.,* 2012].

Figure 8: SP-AMS NR-PM_{BC} vs. HR-AMS NR-PM_1 scatter plots of the SO_4^{2-}, NO_3^-, NH_4^+ and Chl^- mass loadings ($\mu g\ m^{-3}$). The fits to the data are shown by the solid lines. The slopes of the correlation, f(x), and the r^2 are also reported. The dashed lines indicate the fits to similar SP-AMS vs. HR-AMS correlations from the NYC 2009 study.

Figure 9: Panel a: V-HTDMA-based frequency distribution of the number fraction of particles with GF = 1 plotted as a function of the photochemical age proxy (PCA). Most of particles with GF=1 have PCA < 0.4. Panel b: frequency distribution of the SMPS-based TD/ambient surface area (SA). The average SA_{TD}/SA_{AMB} ratio is 0.30, corresponding to ~ 30% of PM_1 mass associated with rBC.

Figure 10: Volatility profiles ("thermograms") for the SP-AMS NR-PM_{BC} species ORG, SO_4^2, NO_3^- and NH_4^+. The data are reported as mass fraction remaining (MFR) as function of the centerline thermal denuder (TD) temperature. The error bars represent the variability in the data (1-σ standard deviation of the measurements).

Figure 11: Thermograms of the SP-AMS NR-PM_{BC} species ORG, SO_4^{2-}, NO_3^-, NH_4^+ and Chl^- (panels a, b), CO_2^+ (panels c, d) and $C_3H_7^+$, $C_4H_9^+$, $C_2H_3O^+$ (panels e, f) for the case studies of May 29 (left) and May 15 (right). On May 15, the CO_2^+ ion has the "expected" volatility profile whereas it remains almost flat in the case of May 29, indicating the presence of refractory, non-volatile organic coating material. The error bars represent the 1−σ standard deviation of the measurements.

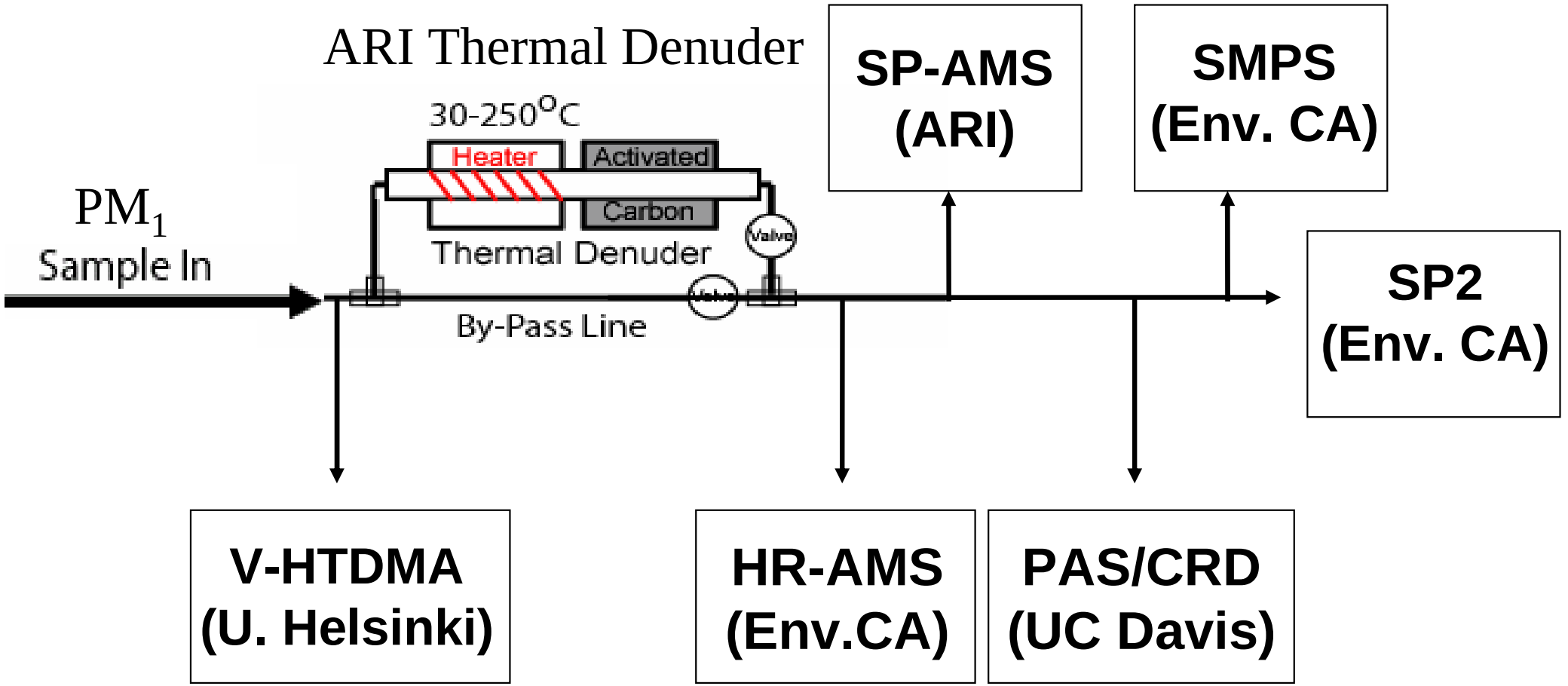
ARI Thermal Denuder
30-250°C
Heater
Activated
Carbon
Thermal Denuder
Valve
Valve
By-Pass Line
PM1
Sample In
SP-AMS
(ARI)
SMPS
(Env. CA)
SP2
(Env. CA)
V-HTDMA
(U. Helsinki)
HR-AMS
(Env.CA)
PAS/CRD
(UC Davis)

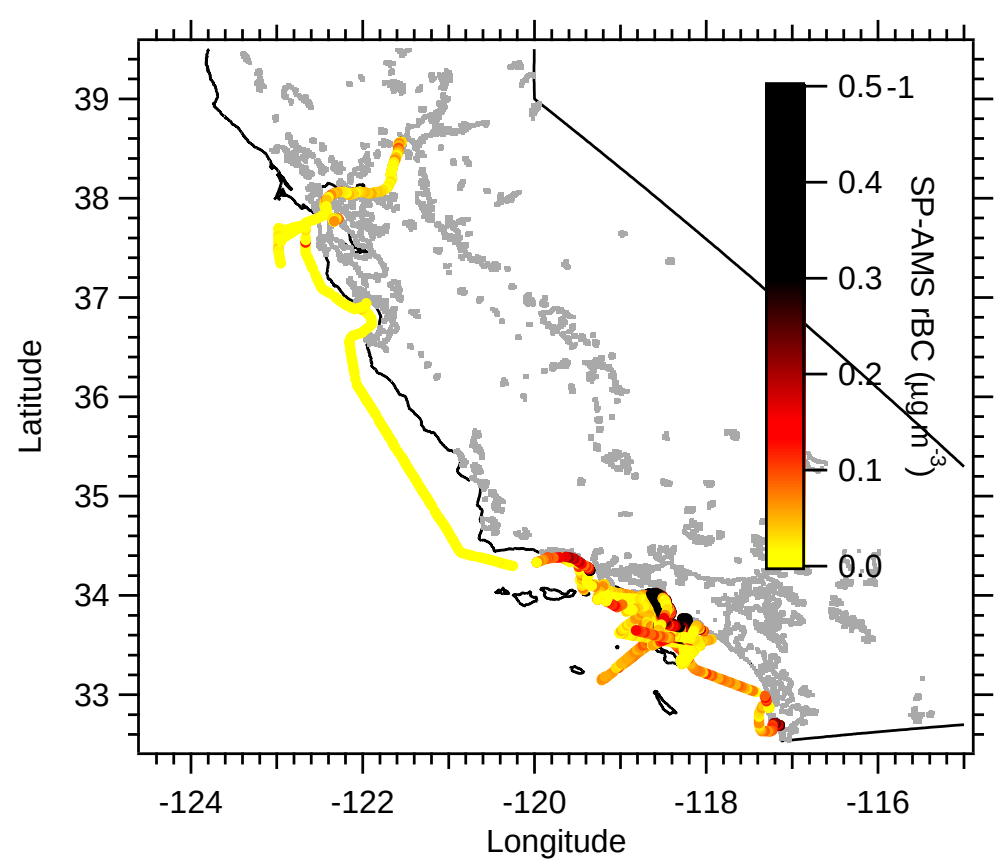
Latitude
39
38
37
36
35
34
33
-124
-122
-120
-118
-116
Longitude
SP-AMS rBC (μg m-3)
0.5
-1
0.4
0.3
0.2
0.1
0.0

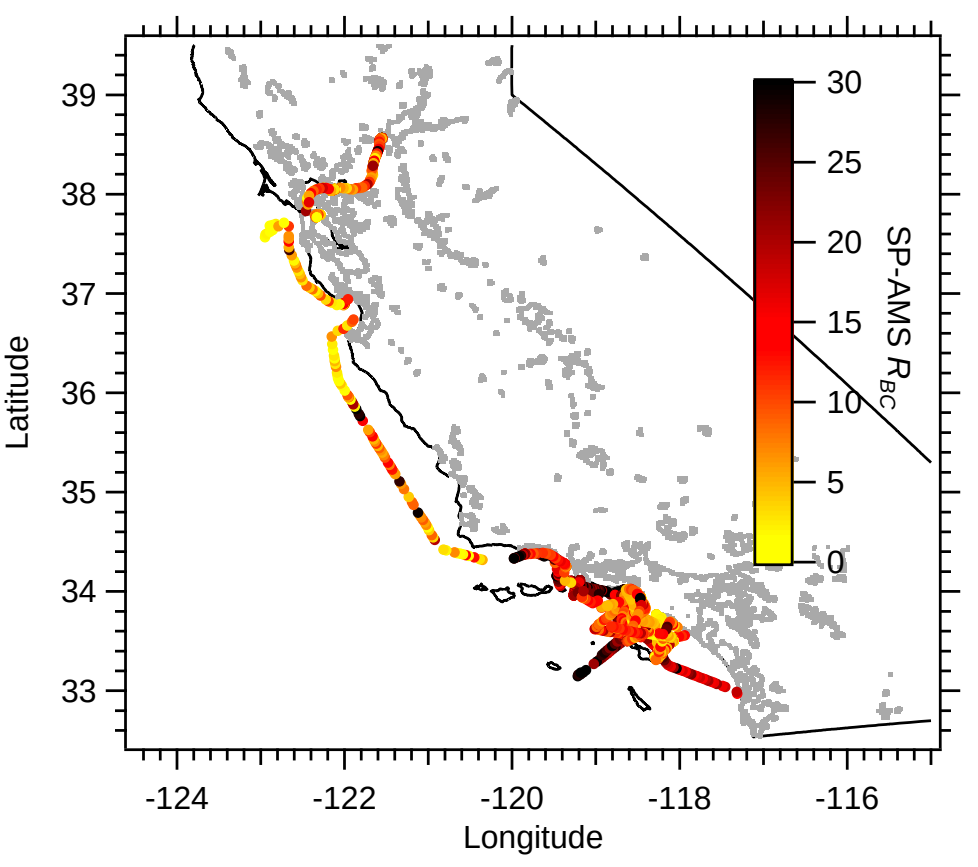
Latitude
39
38
37
36
35
34
33
-124
-122
-120
-118
-116
Longitude
SP-AMS R_{BC}
30
25
20
15
10
5
0

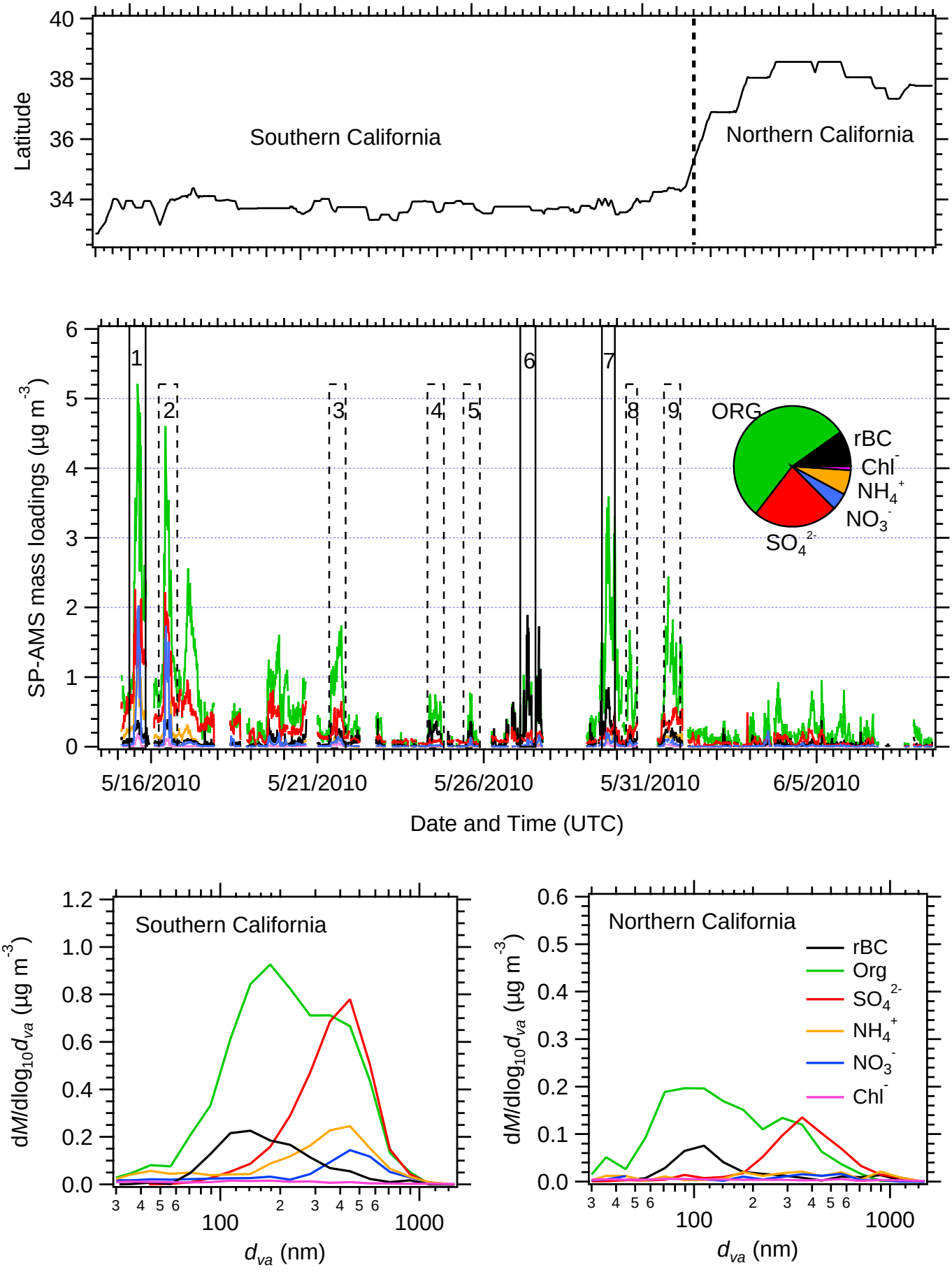
Latitude
40
38
36
34
Southern California
Northern California
SP-AMS mass loadings (μg m-3)
6
5
4
3
2
1
0
1
2
3
4
5
6
7
8
9
ORG
rBC
Chl-
NH4+
NO3-
SO4 2-
5/16/2010
5/21/2010
5/26/2010
5/31/2010
6/5/2010
Date and Time (UTC)
Southern California
dM/dlog10dva (μg m-3)
1.2
1.0
0.8
0.6
0.4
0.2
0.0
3 4 5 6
100
2 3 4 5 6
1000
dva (nm)
Northern California
rBC
Org
SO4 2-
NH4+
NO3-
Chl-
0.6
0.5
0.4
0.3
0.2
0.1
0.0
3 4 5 6
100
2 3 4 5 6
1000
dva (nm)

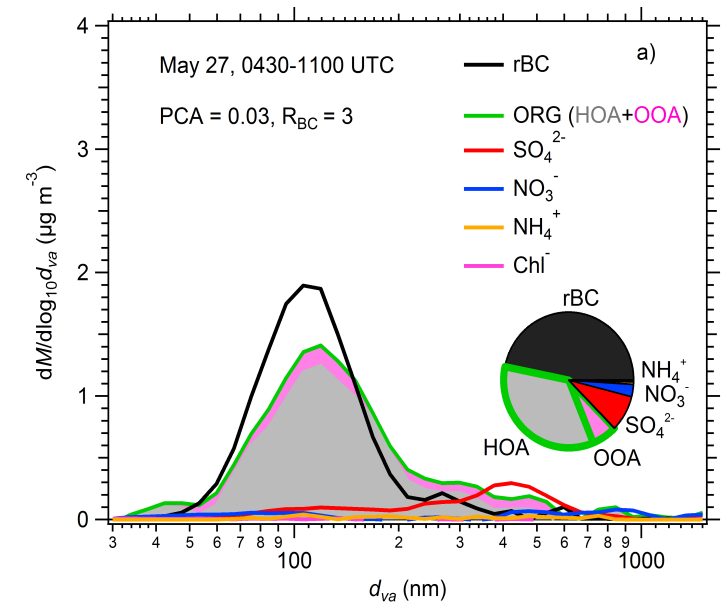
May 27, 0430-1100 UTC
PCA = 0.03, R_BC = 3
a)
rBC
ORG (HOA+OOA)
SO4 2-
NO3 -
NH4 +
Chl -
rBC
NH4 +
NO3 -
SO4 2-
HOA
OOA
dM/dlog10dva (µg m-3)
dva (nm)

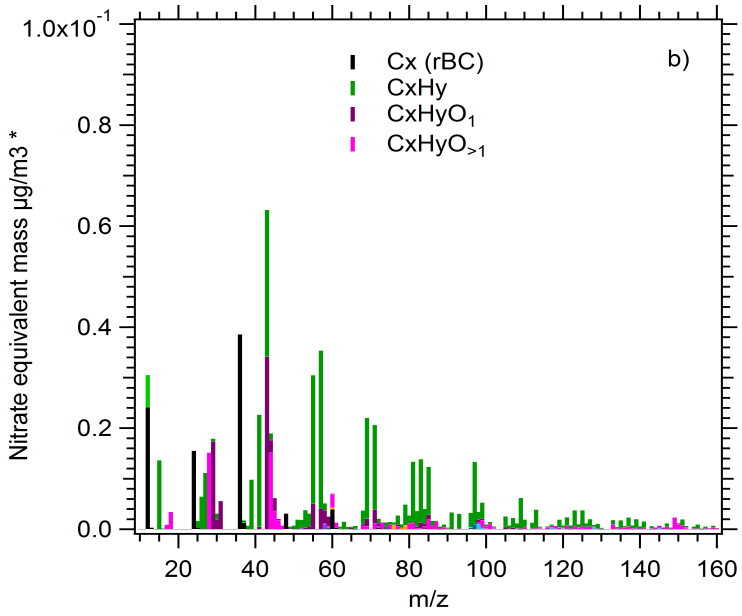
b)
Cx (rBC)
CxHy
CxHyO1
CxHyO>1
Nitrate equivalent mass µg/m3 *
m/z

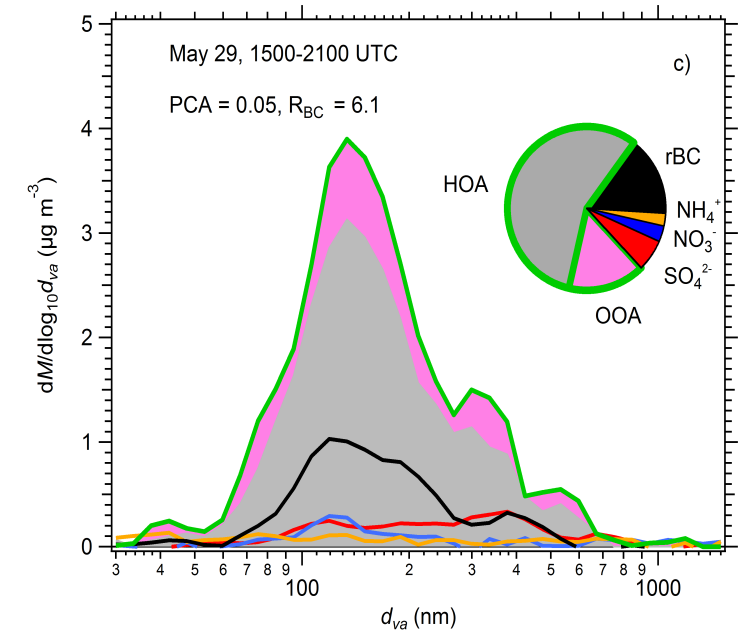
May 29, 1500-2100 UTC
PCA = 0.05, R_BC = 6.1
c)
HOA
rBC
NH4 +
NO3 -
SO4 2-
OOA
dM/dlog10dva (µg m-3)
dva (nm)

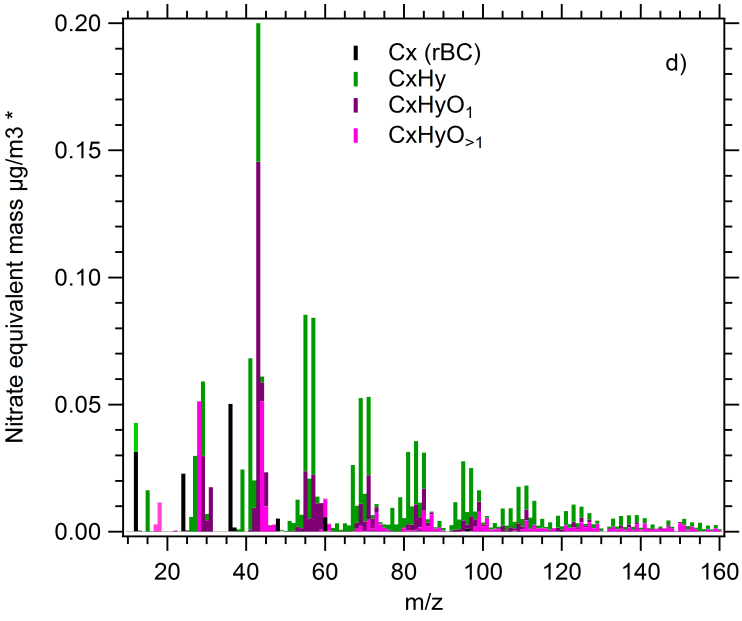
d)
Cx (rBC)
CxHy
CxHyO1
CxHyO>1
Nitrate equivalent mass µg/m3 *
m/z

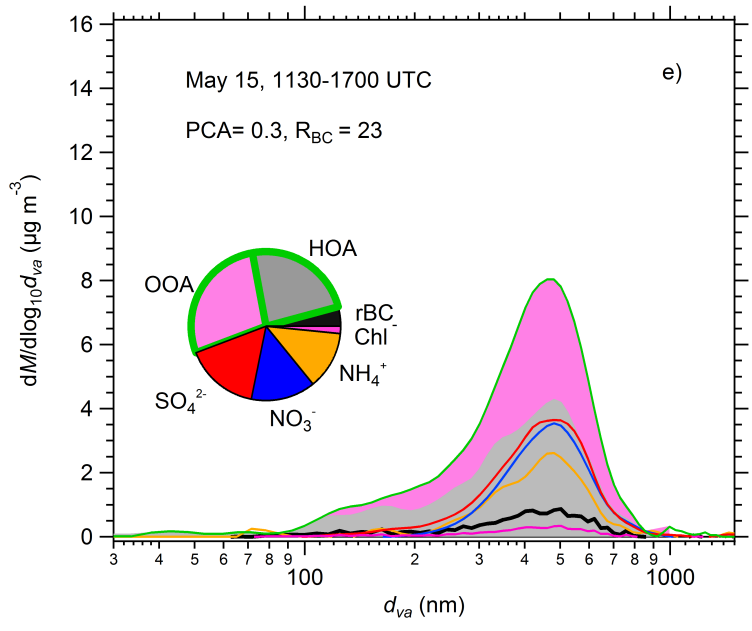
May 15, 1130-1700 UTC
PCA= 0.3, R_BC = 23
e)
HOA
OOA
rBC
Chl -
NH4 +
SO4 2-
NO3 -
dM/dlog10dva (µg m-3)
dva (nm)

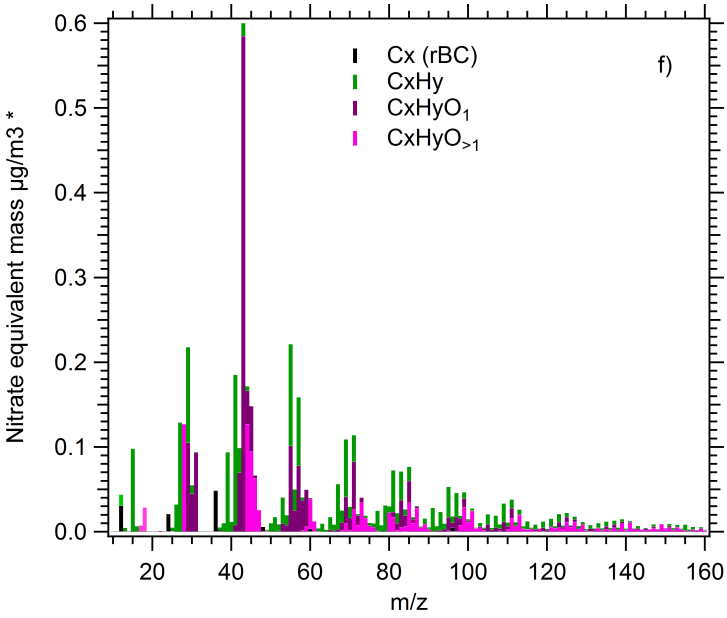
f)
Cx (rBC)
CxHy
CxHyO1
CxHyO>1
Nitrate equivalent mass µg/m3 *
m/z

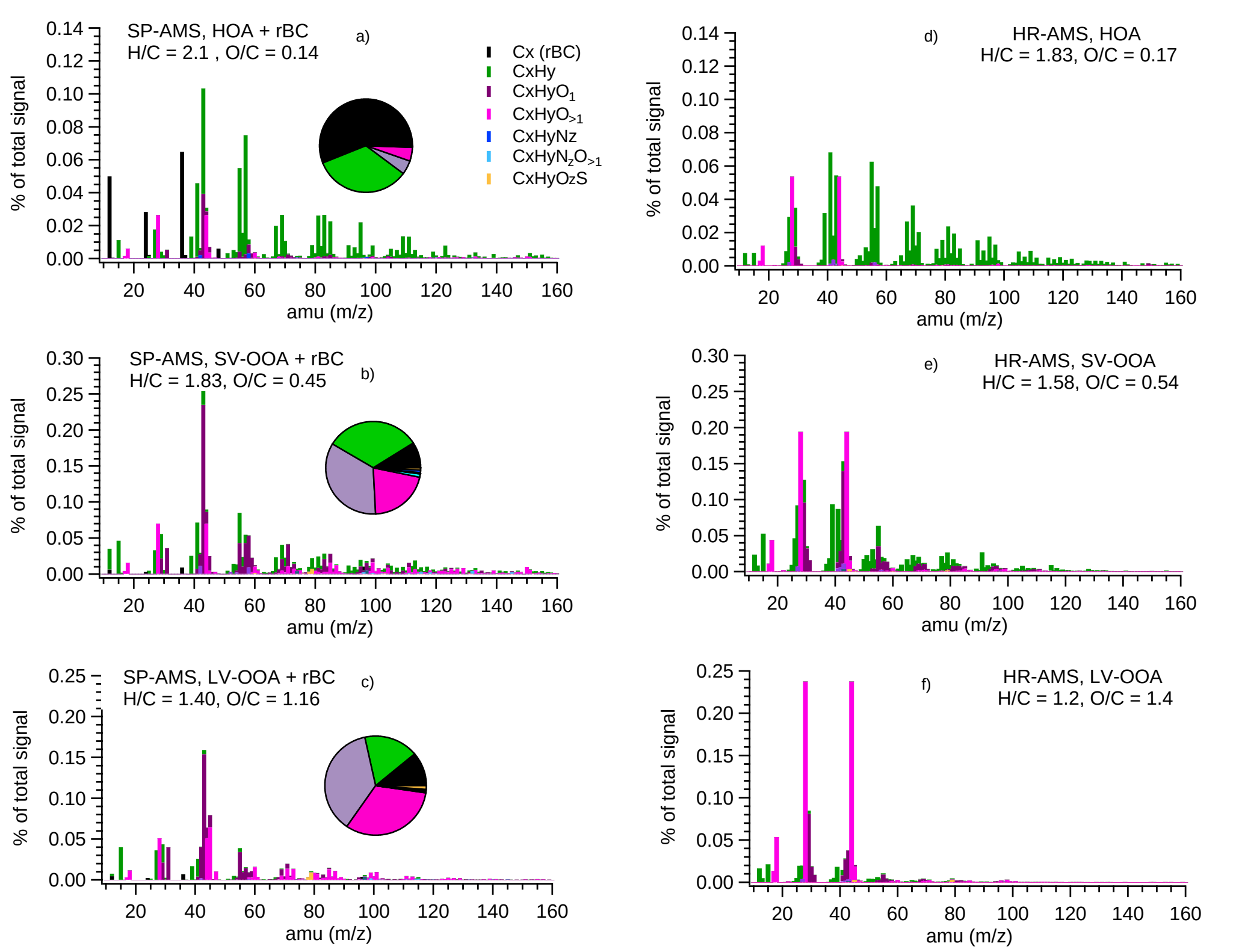
SP-AMS, HOA + rBC
H/C = 2.1 , O/C = 0.14
a)
Cx (rBC)
CxHy
CxHyO1
CxHyO>1
CxHyNz
CxHyNzO>1
CxHyOzS
% of total signal
amu (m/z)
SP-AMS, SV-OOA + rBC
H/C = 1.83, O/C = 0.45
b)
SP-AMS, LV-OOA + rBC
H/C = 1.40, O/C = 1.16
c)
HR-AMS, HOA
H/C = 1.83, O/C = 0.17
d)
HR-AMS, SV-OOA
H/C = 1.58, O/C = 0.54
e)
HR-AMS, LV-OOA
H/C = 1.2, O/C = 1.4
f)

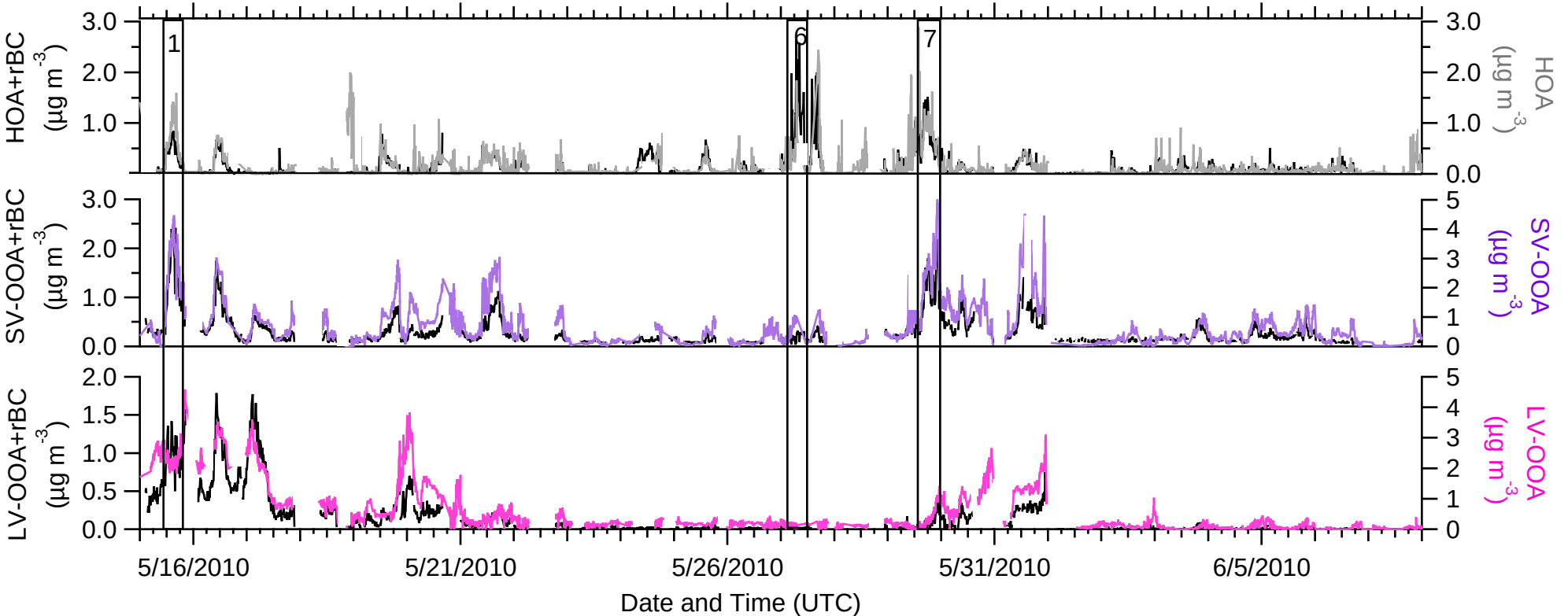
HOA+rBC (μg m-3)
SV-OOA+rBC (μg m-3)
LV-OOA+rBC (μg m-3)
HOA (μg m-3)
SV-OOA (μg m-3)
LV-OOA (μg m-3)
1
6
7
5/16/2010
5/21/2010
5/26/2010
5/31/2010
6/5/2010
Date and Time (UTC)

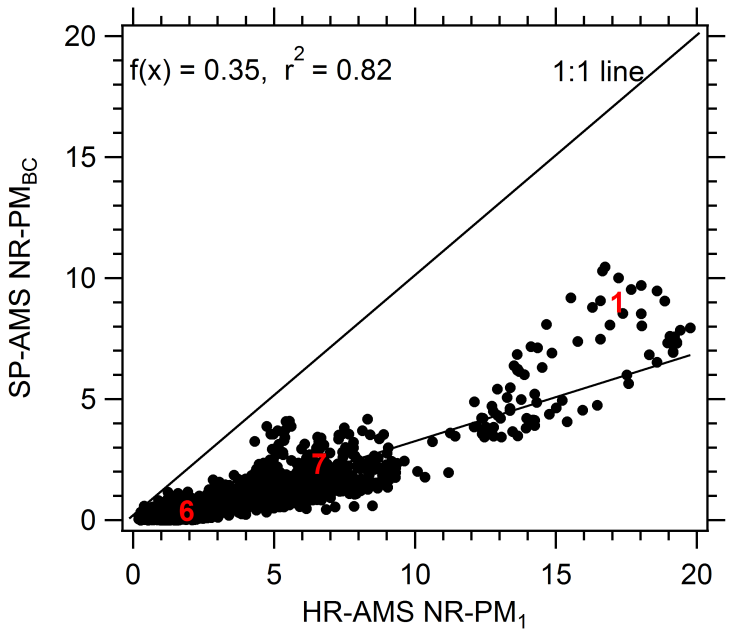
f(x) = 0.35, r2 = 0.82
1:1 line
1
7
6
SP-AMS NR-PMBC
HR-AMS NR-PM1
0
5
10
15
20

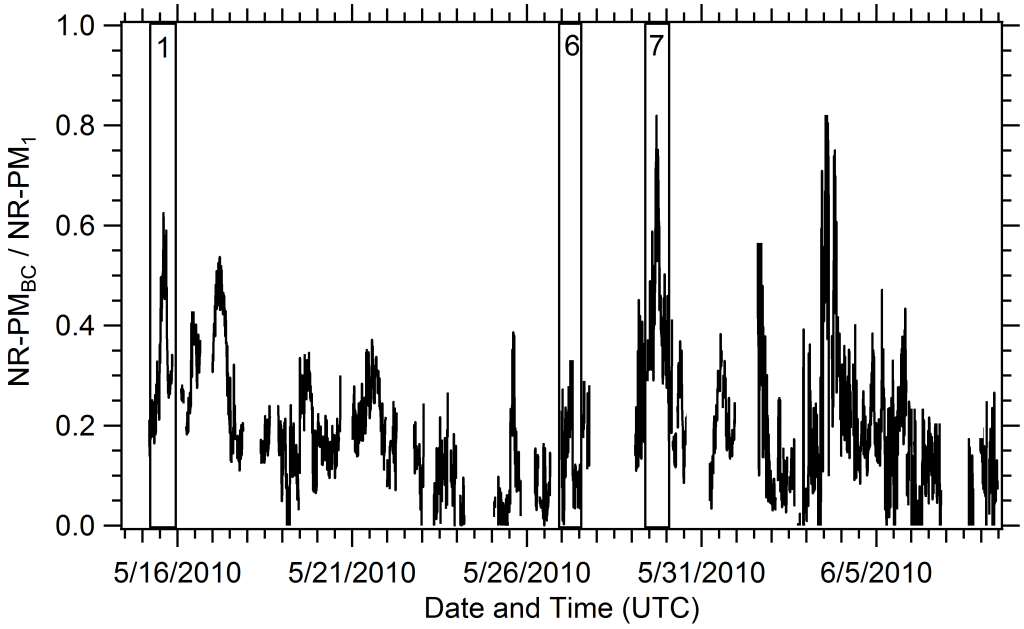
1
6
7
NR-PMBC / NR-PM1
0.0
0.2
0.4
0.6
0.8
1.0
5/16/2010
5/21/2010
5/26/2010
5/31/2010
6/5/2010
Date and Time (UTC)

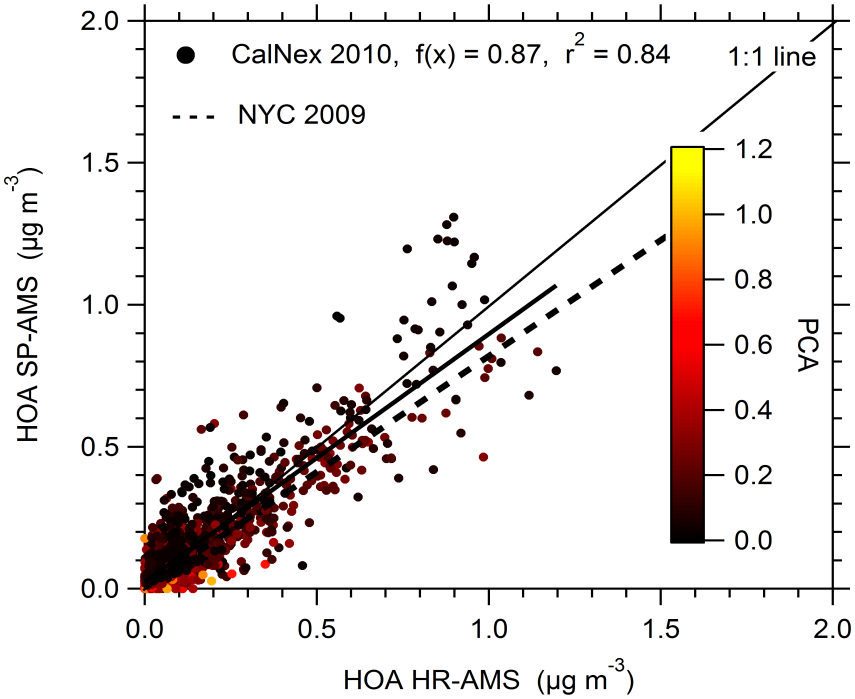
CalNex 2010, f(x) = 0.87, r2 = 0.84
1:1 line
NYC 2009
PCA
HOA SP-AMS (µg m-3)
HOA HR-AMS (µg m-3)
0.0
0.5
1.0
1.5
2.0

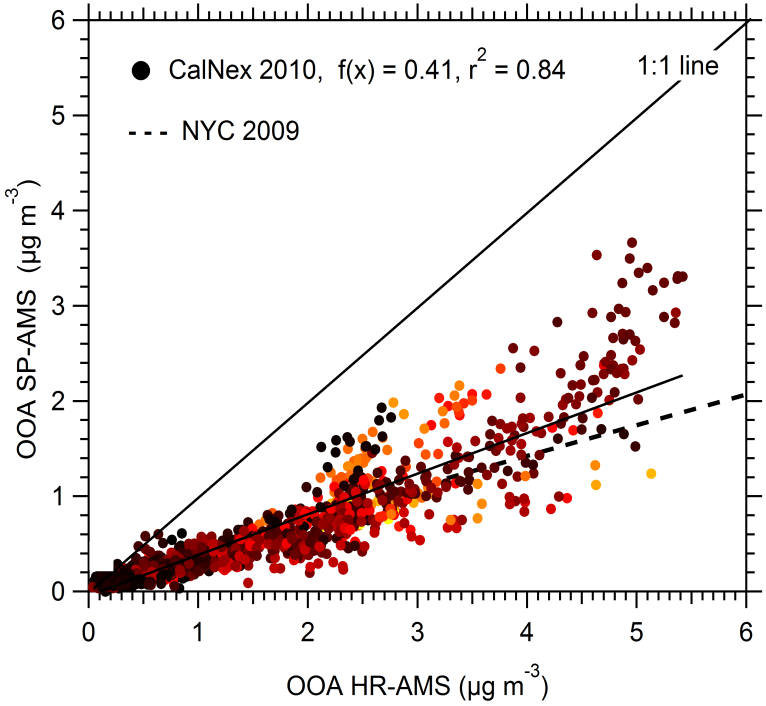
CalNex 2010, f(x) = 0.41, r2 = 0.84
1:1 line
NYC 2009
OOA SP-AMS (µg m-3)
OOA HR-AMS (µg m-3)
0
1
2
3
4
5
6

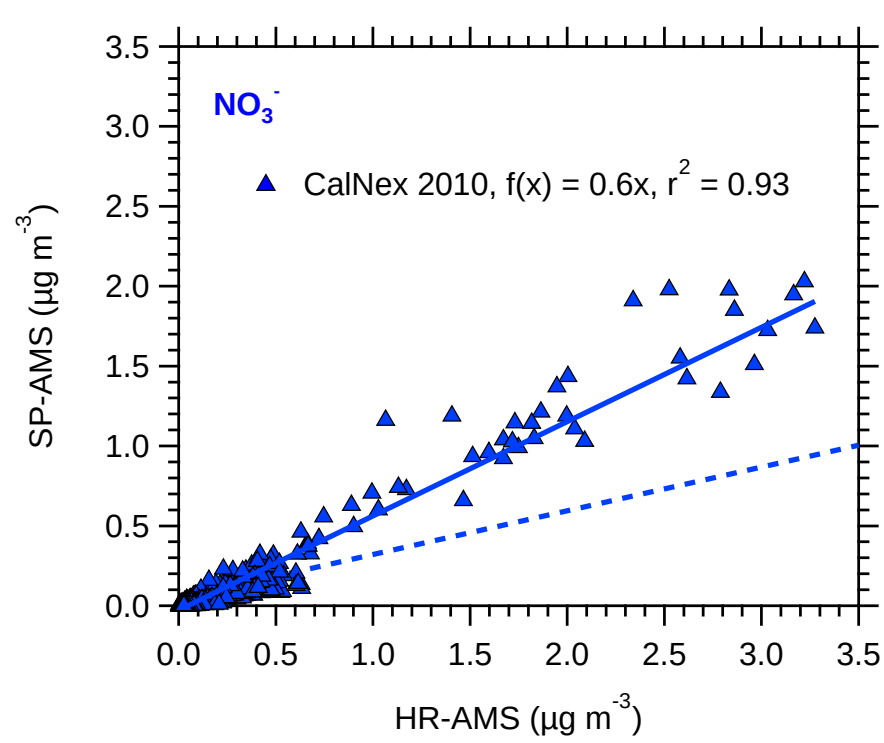
NO3-
CalNex 2010, f(x) = 0.6x, r2 = 0.93
SP-AMS (µg m-3)
HR-AMS (µg m-3)
0.0
0.5
1.0
1.5
2.0
2.5
3.0
3.5

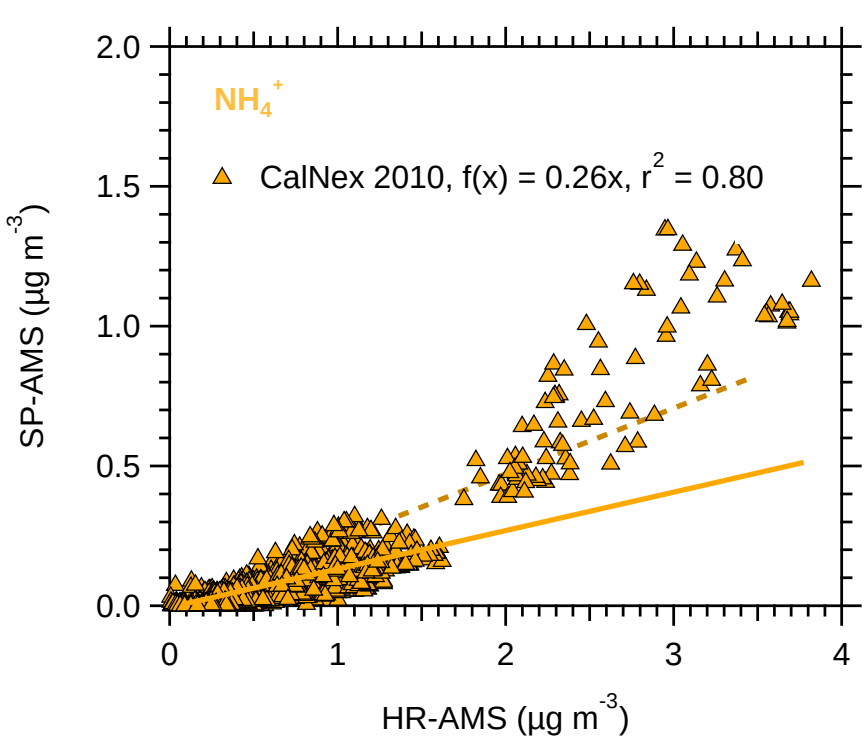
NH4+
CalNex 2010, f(x) = 0.26x, r2 = 0.80
SP-AMS (µg m-3)
HR-AMS (µg m-3)
0.0
0.5
1.0
1.5
2.0
0
1
2
3
4

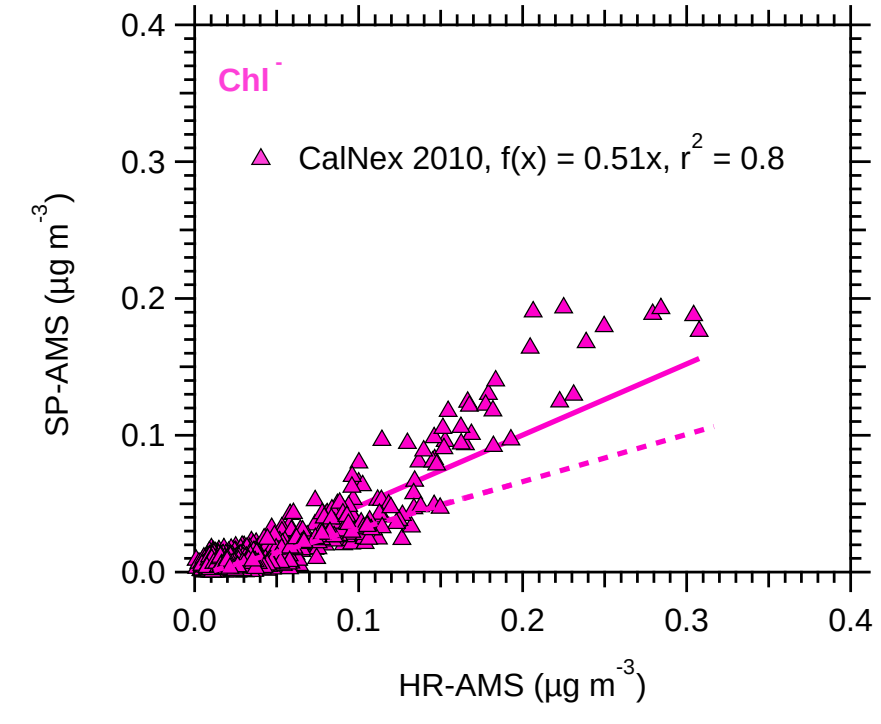
Chl-
CalNex 2010, f(x) = 0.51x, r2 = 0.8
SP-AMS (µg m-3)
HR-AMS (µg m-3)
0.0
0.1
0.2
0.3
0.4

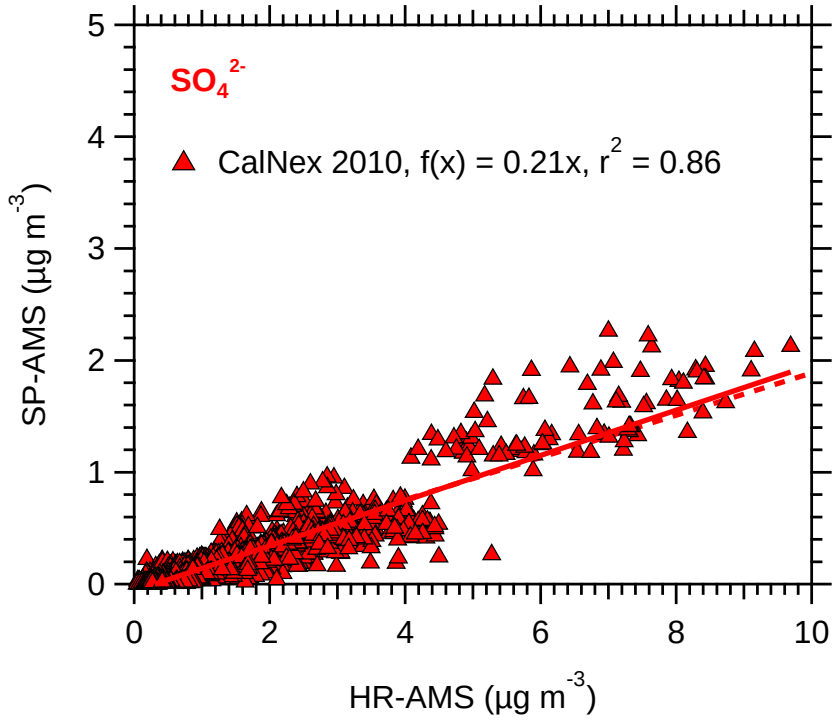
SO4 2-
CalNex 2010, f(x) = 0.21x, r2 = 0.86
SP-AMS (µg m-3)
HR-AMS (µg m-3)
0
1
2
3
4
5
0
2
4
6
8
10

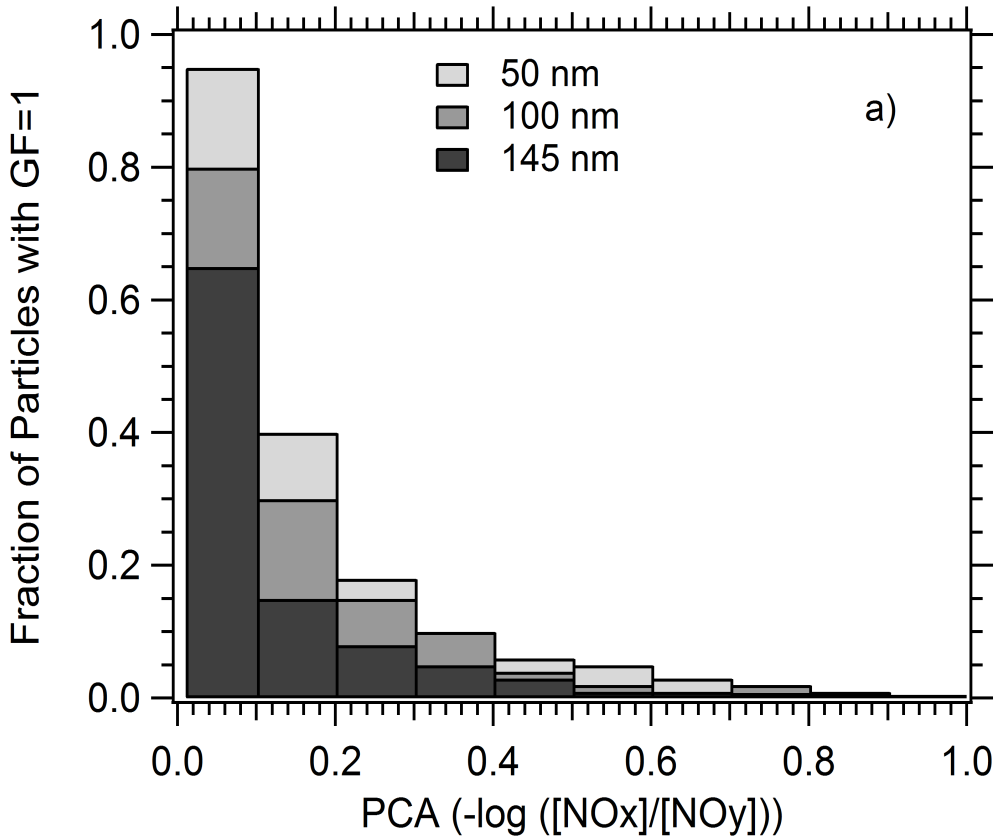
Fraction of Particles with GF=1
1.0
0.8
0.6
0.4
0.2
0.0
50 nm
100 nm
145 nm
a)
0.0
0.2
0.4
0.6
0.8
1.0
PCA (-log ([NOx]/[NOy]))

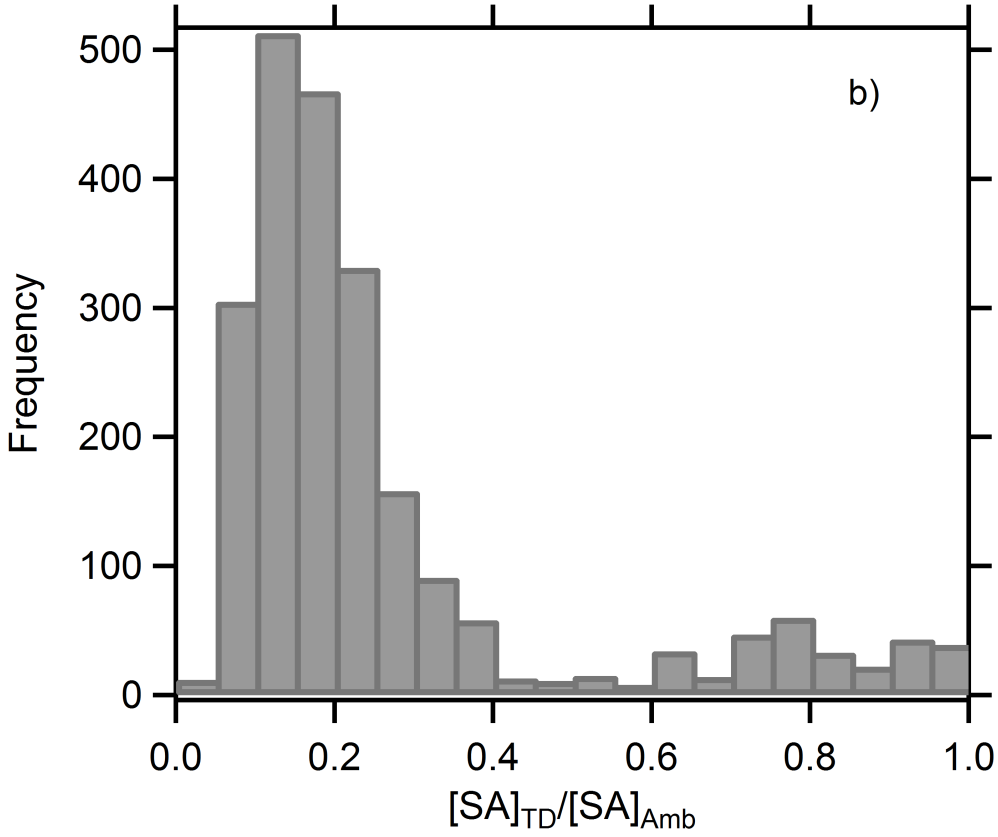
Frequency
500
400
300
200
100
0
b)
0.0
0.2
0.4
0.6
0.8
1.0
[SA]TD/[SA]Amb

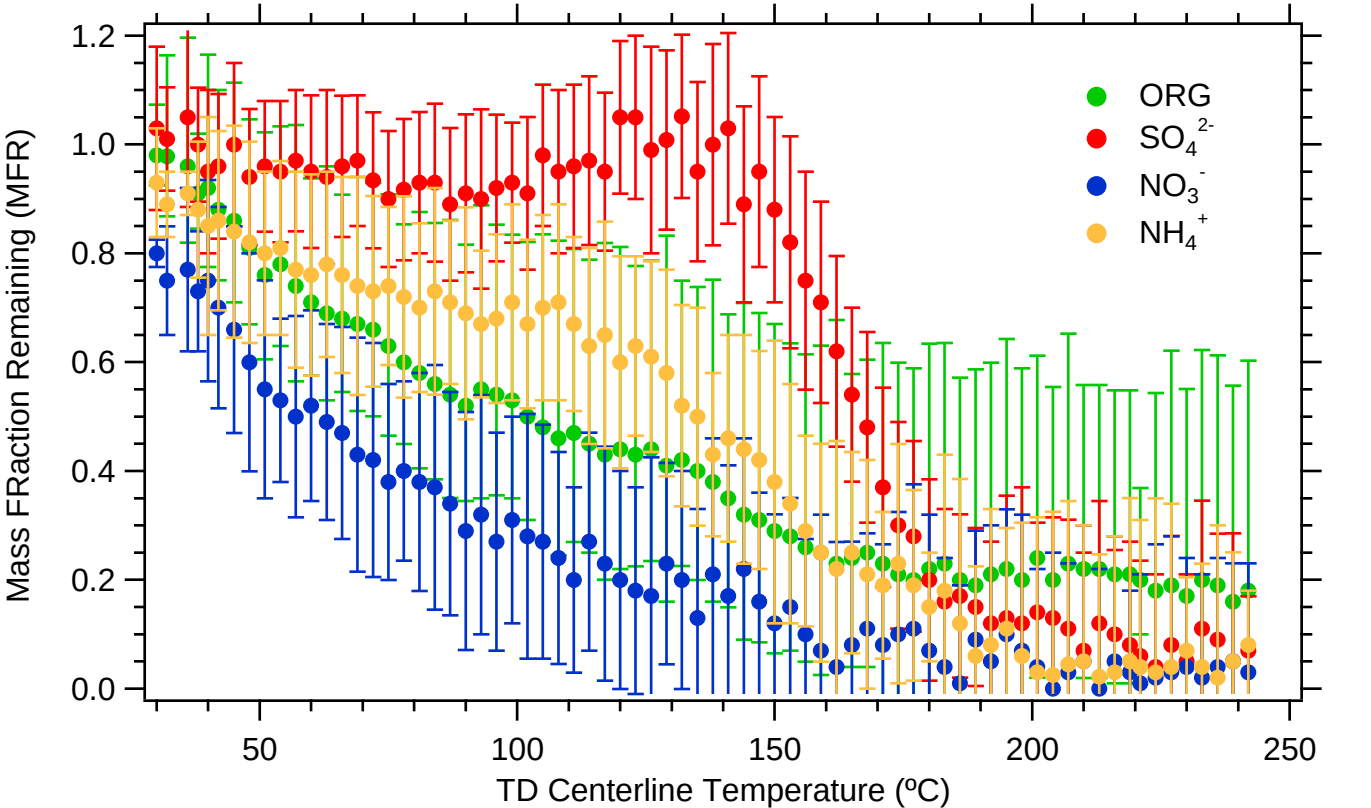
Mass FRaction Remaining (MFR)
1.2
1.0
0.8
0.6
0.4
0.2
0.0
50
100
150
200
250
TD Centerline Temperature (ºC)
ORG
SO4 2-
NO3 -
NH4 +

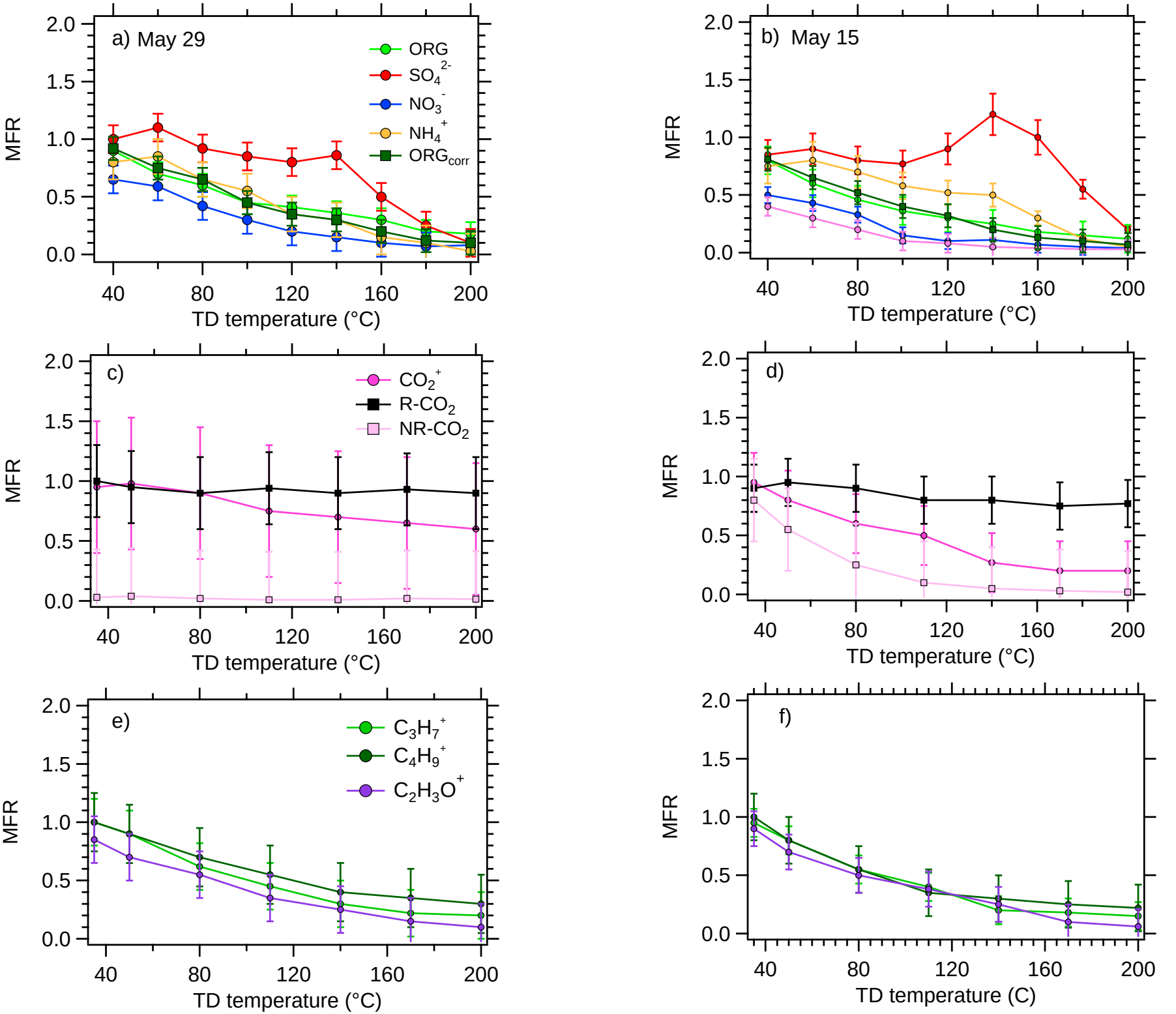
a) May 29
ORG
SO4 2-
NO3 -
NH4 +
ORGcorr
MFR
TD temperature (°C)
b) May 15
MFR
TD temperature (°C)
c)
CO2 +
R-CO2
NR-CO2
MFR
TD temperature (°C)
d)
MFR
TD temperature (°C)
e)
C3H7 +
C4H9 +
C2H3O +
MFR
TD temperature (°C)
f)
MFR
TD temperature (C)